KeA1

CHINESE ROOTS
GLOBAL IMPACT

Contents lists available at ScienceDirect

Petroleum Science





Original Paper

Bayesian AVO inversion of fluid and anisotropy parameters in VTI media using IADR-Gibbs algorithm



Ying-Hao Zuo ^{a, b, c, d}, Zhao-Yun Zong ^{a, b, c, *}, Xing-Yao Yin ^{a, b, c}, Kun Li ^e, Ya-Ming Yang ^{a, b, c}, Si Wu ^f

- ^a State Key Laboratory of Deep Oil and Gas, China University of Petroleum (East China), Qingdao, 266580, Shandong, China
- ^b School of Geosciences, China University of Petroleum (East China), Qingdao, 266580, Shandong, China
- ^c Laoshan Laboratory, Qingdao, 266580, Shandong, China
- ^d Department of Physics, University of Alberta, Edmonton, T6G2E1, Alberta, Canada
- ^e College of Computer Science and Technology, China University of Petroleum (East China), Qingdao, 266580, Shandong, China
- f SINOPEC Geophysical Research Institute Co., Ltd, Nanjing, 211103, Jiangsu, China

ARTICLE INFO

Article history: Received 28 October 2024 Received in revised form 6 February 2025 Accepted 9 May 2025 Available online 16 May 2025

Edited by Meng-Jiao Zhou

Keywords: Fluid and anisotropy parameters AVO inversion Bayesian framework Probabilistic inversion

ABSTRACT

Fluid identification and anisotropic parameters characterization are crucial for shale reservoir exploration and development. However, the anisotropic reflection coefficient equation, based on the transverse isotropy with a vertical axis of symmetry (VTI) medium assumption, involves numerous parameters to be inverted. This complexity reduces its stability and impacts the accuracy of seismic amplitude variation with offset (AVO) inversion results. In this study, a novel anisotropic equation that includes the fluid term and Thomsen anisotropic parameters is rewritten, which reduces the equation's dimensionality and increases its stability. Additionally, the traditional Markov Chain Monte Carlo (MCMC) inversion algorithm exhibits a high rejection rate for random samples and relies on known parameter distributions such as the Gaussian distribution, limiting the algorithm's convergence and sample randomness. To address these limitations and evaluate the uncertainty of AVO inversion, the IADR-Gibbs algorithm is proposed, which incorporates the Independent Adaptive Delayed Rejection (IADR) algorithm with the Gibbs sampling algorithm. Grounded in Bayesian theory, the new algorithm introduces support points to construct a proposal distribution of non-parametric distribution and reselects the rejected samples according to the Delayed Rejection (DR) strategy. Rejected samples are then added to the support points to update the proposal distribution function adaptively. The equation rewriting method and the IADR-Gibbs algorithm improve the accuracy and robustness of AVO inversion. The effectiveness and applicability of the proposed method are validated through synthetic gather tests and practical data applications. © 2025 The Authors. Publishing services by Elsevier B.V. on behalf of KeAi Communications Co. Ltd. This

© 2025 The Authors. Publishing services by Elsevier B.V. on behalf of KeAi Communications Co. Ltd. This is an open access article under the CC BY-NC-ND license (http://creativecommons.org/licenses/by-nc-nd/4.0/).

1. Introduction

Shale reservoirs typically display characteristics of VTI media (Jones and Wang, 1981; Banik, 1984). The anisotropy of VTI media, resulting from the finely layered sedimentary structures and the aligned mineral composition, influences the seismic AVO response (Crampin, 1981; Zhang et al., 2019; Lang et al., 2023). Considering the impact of VTI anisotropy, precise inversion of fluid term and anisotropic parameters establishes a theoretical basis for

* Corresponding author.

E-mail address: zongzhaoyun@upc.edu.cn (Z.-Y. Zong).

Peer review under the responsibility of China University of Petroleum (Beijing).

identifying and mapping the spatial distribution of fluids within shale reservoirs and underpins the exploration and extraction of unconventional hydrocarbons.

The fluid factor, or fluid indicator, is a key parameter that characterizes fluid properties within the reservoir, playing a vital role in the interpretation of oil and gas reservoirs and fluid identification (Pan et al., 2019). Smith and Gidlow (1987) introduced the fluid factor concept, formulating it as a function of the rate of change in P-wave and S-wave velocities. Building on Biot and Gassmann's theory of saturated porous rocks, Russell et al. (2003, 2011) defined the fluid term as the difference between the product of rock density and the square of P-wave velocity, and the product of density and the square of S-wave velocity. The definition leads to

the derivation of a broadly utilized approximate reflection coefficient equation. Yin and Zhang (2014) employed a linear approximation to separate the fluid term into the fluid bulk modulus, coining it as the fluid indicator factor. Chen et al. (2018) suggested that the ratio of the fluid term to porosity constitutes the fluid factor. Feng et al. (2024) reformulated the fluid term by expressing it in terms of the porosity and fluid bulk modulus, applying it in frequency-dependent inversion in HTI media. Given that the fluid factor is influenced by various elements such as reservoir and fluid types, lithology, and pressure, it does not represent a singular parameter. Instead, it is essential to deduce specific fluid factors that accurately represent fluid types for a given study area, involving a combination of different parameters, such as Poisson's ratio, Poisson's impedance, and fluid bulk modulus (Li et al., 2022; Ma et al., 2023; Feng et al., 2024; Chen et al., 2024b). In our research, Russell's fluid term is adapted as the fluid factor to develop a reliable seismic forward model.

The stability and precision of the forward operator significantly influence the robustness and accuracy of prestack seismic inversion in VTI media (Zong and Yin, 2017; Zong and Sun, 2022; Chen and Zong, 2022). Seismic forward operators comprise both exact and approximate seismic reflection coefficient equations, along with seismic wavelets. Numerous scholars propose VTI media's exact reflection coefficient equation (Daley and Hron, 1977; Carcione, 1997; Graebner, 1992; Schoenberg and Protazio, 1992). The exact equation offers an accurate representation of the relationship between model parameters and seismic data. However, it is characterized by a multitude of parameters, intricate formulation, and pronounced nonlinearity. This complexity leads to significant uncertainty and diminished computational efficiency when directly applied to inversion processes. To address these challenges, many researchers introduce approximate equations for VTI media predicated based on the premises of weak anisotropy and weak contrast interfaces (Ursin and Haugen, 1996; Rüger, 1998; Vavrycuk and Psencík, 1998). Notably, Thomsen (1986) introduced the anisotropy parameter, also referred to as the Thomsen anisotropy parameter, based on the weakly anisotropic medium assumption, leading to the derivation of a linearized anisotropic reflectivity approximate equation. Rüger (1998) further developed a novel approximate reflectivity equation to overcome the limitations of Thomsen's equation at large incidence angles. Additionally, simplified approximate equations are utilized for AVO or AVA inversion due to their straightforward expressions (Plessix and Bork, 2000; Zhang and Li, 2013; Lin and Thomsen, 2013; Lu et al., 2018; Zhou et al., 2020; Yang et al., 2023; Fu, 2024). The approximate reflection coefficient equation reduces the complexity of the equation and improves its stability. The approximate equation for VTI media typically involves five parameters, potentially exacerbating the ill-condition of the equation. The differing contributions of isotropic and anisotropic parameters to the equation can lead to instability and multiple solutions during simultaneous inversion. Luo et al. (2020) proposed a stepwise inversion strategy to mitigate these issues, although this approach may introduce significant cumulative errors. A more effective solution involves the equation rewriting method, which consolidates parameter terms with identical coefficients, merging less influential Thomsen parameters into isotropic parameter terms (Zhang et al., 2019; Ge et al., 2021). In this study, an approximate reflection coefficient equation is derived incorporating the fluid term, shear modulus, density, and Thomsen anisotropic parameters, simplifying the five parameters into three combined attribute parameters. Given the complexity of VTI media, achieving stable inversion of fluid term and Thomsen anisotropic parameters necessitates a stable forward operator and an appropriate AVO inversion algorithm.

The seismic AVO inversion algorithms for VTI medium primarily include deterministic and statistical inversion algorithms. Deterministic inversion methods utilize various optimization algorithms to identify the optimal solution. However, the VTI approximate reflection coefficient equation has strong nonlinearity, which makes the deterministic inversion algorithm difficult to solve and easily falls into the local optimal solution. Statistical inversion algorithms, founded on Bayesian theory, address the inversion challenge by constructing the posterior probability density distribution function (pdf) of model parameters, thereby quantifying the uncertainty of inversion results (Buland and Omre, 2003; Li et al., 2022; Grana et al., 2022; Yu et al., 2023; Chen et al., 2024a). The maximum a posteriori probability (MAP) algorithm, a widely adopted probabilistic approach, selects the solution with the highest posterior probability as the inverse solution (Marroquin, 1985; Mosegaard and Tarantola, 1995; Luo et al., 2021). Nevertheless, the MAP algorithm's efficiency and accuracy decline when dealing with complex or non-explicit posterior pdf. To overcome these limitations, the MCMC algorithm randomly samples the proposal distribution with the suitable Markov chain to ensure it converges to the target posterior pdf when reaching a detailed stable state. It is a global optimization statistical inversion algorithm that can obtain the global optimal solution of the inversion parameters (Sambridge and Mosegaard, 2002). However, the conventional MCMC algorithm, using the Metropolis and Metropolis-Hastings acceptance-rejection criteria, exhibits a high sample rejection rate (Liang et al., 2011; Baffoun et al., 2017). In addition, the traditional MCMC algorithm typically relies on simple probability distributions like the Gaussian and Cauchy distributions. limiting the randomness of parameter sampling (Ayani and Grana, 2020). The high rejection probability and the known parameter distribution function reduce the algorithm convergence and accuracy of AVO inversion. To solve the above problem, the Independent Adaptive Delayed Rejection (IADR) algorithm integrated with Gibbs sampling is proposed. It establishes a linear piecewise function from the support points and uses it as the proposal distribution of the non-parametric distribution. The approach, combined with Gibbs sampling and a delayed rejection strategy, allows for the acceptance of initially rejected samples with a certain probability and the randomly simulation independent sample points for the proposal distribution. The sample points rejected again are added to new support points, which are used to update the proposal distribution adaptively.

In this research, a novel approximate reflection coefficient equation for VTI media is introduced, formulated with three synthesized attribute parameters that encapsulate fluid term, shear modulus, density, and Thomsen's anisotropy parameter. The comparison of the condition number and the approximate and exact equations verifies the stability and accuracy of the derived equation. Furthermore, the improved IADR algorithm, integrated with Gibbs sampling, is proposed to address the high rejection rates encountered in traditional MCMC algorithms and the constraints on random sampling due to predefined parameter distributions. The efficacy of the proposed inversion method is corroborated through the application of synthetic gathers and real data.

2. Theory

2.1. Derivation and rewriting of the anisotropic reflection coefficient equation

After deriving and rewriting the equation, a novel approximate reflectivity equation for VTI media is expressed as:

$$\begin{split} R_{\mathrm{pp}}(\theta) &= \frac{1}{4} k_1 \, \ln \left[\frac{(A)_{i+1}}{(A)_i} \right] - k_3 \, \sin^2 \theta \, \ln \left[\frac{(B)_{i+1}}{(B)_i} \right] \\ &+ \frac{1}{4} k_1 \, \tan^2 \theta \, \ln \left[\frac{(C)_{i+1}}{(C)_i} \right], \end{split} \tag{1}$$

where

$$A = f \mu^{\frac{k_2}{k_1}} \rho^{\frac{1}{k_1}}, B = \mu e^{\frac{1}{2k_3} \varepsilon - \frac{1}{2k_3} \delta}, C = f \mu^{\frac{k_2}{k_1}} e^{\frac{2}{k_1} \varepsilon} / \rho^{\frac{1}{k_1}}.$$
 (2)

Appendix A shows the specific derivation and simplification of Eq. (1). A represents the combined parameter of fluid term, shear modulus, and density. B represents the combined parameter of shear modulus and Thomsen anisotropy parameters. C represents the combined parameter of fluid term, shear modulus, density and Thomsen anisotropy parameter ε . Its correlation with A is determined by ε . The rewritten Eq. (1) will be called the new equation, and Eq. (A-12) without parameter merging and equation rewriting will be called the original equation.

To verify the precision of the new equation, a four-layer model representing four types of AVO is constructed, with the corresponding isotropic and anisotropic parameters detailed in Table 1. Fig. 1 shows that new equation is close to Ruger's approximate VTI equation and the exact VTI equation based on the model parameters for the four AVO types, particularly at small incident angles. The congruence of equations confirms the suitability of the new equation for prestack seismic inversion.

Fig. 2 demonstrates a comparison of the condition numbers for the coefficient matrices of the new equation and the original equation. The blue circle denotes the condition number for the coefficient matrix of the original equation, while the red circle signifies the condition number for the new equation. Notably, the condition number for the new equation is significantly lower than that of the original equation and diminishes as the maximum incident angle increases. The trend suggests that the new equation becomes more stable and the inversion more precise with larger incident angles.

The effect of changes in model parameters on the reflection coefficient based on the new equation and the original equation are shown in Figs. 3 and 4. Fig. 3 indicates that at small incident angles, the fluid term, shear modulus, and density significantly influence the reflection coefficient, whereas the impact of the Thomsen anisotropy parameter ε is minimal. The inversion result of ε based on small-angle seismic data is unreliable and should be combined with large-angle seismic data for inversion. Conversely, in the case of the large incident angle, the density contribution is low increasing the difficulty of inversion. Fig. 4 shows that when the incident angle is small, the attribute parameters B and C have a certain contribution to the reflection coefficient. When the incident angle is large, the contribution of attribute parameters A, B, and C is large. The contribution of B is greater than that of C. Similarly, the contribution of C is greater than that of A. The different contributions of the three attribute parameters indicate that the new equation applies to prestack seismic direct inversion and can be

Table 1 Model parameters of a four-layer theoretical model.

Layer	V _p , m/s	V _s , m/s	ρ , kg/m ³	ε	δ
1	5000	3000	2400	0	0
2-1	6000	4000	2400	0.07	0.05
2-2	5100	3300	2400	0.07	0.05
2-3	3900	2850	2400	0.07	0.05
2-4	3900	2550	2400	0.07	0.05

inverted to obtain accurate inversion profiles. In addition, for the sake of comparison, Fig. 5 shows the reflection coefficient of attribute parameter B and Thomsen anisotropy parameter E in the red dashed area. When the incident angle is between 0° and 12° , the contribution of E to the reflection coefficient is small, while the contribution of E is large. This shows that the method of parameter merging is used to couple the Thomsen anisotropy parameter with a small contribution and the isotropy parameter with a large contribution as a combined parameter to improve the contribution of parameters, thereby increasing the inversion accuracy.

2.2. IADR-Gibbs seismic inversion

The equation of the inverted parameters y and the prestack seismic data $D(\theta)$ is defined as:

$$D(\theta) = l(\theta) * R_{pp}(\theta, y) + r, \tag{3}$$

where y refers to [A,B,C], $l(\theta)$ denotes wavelet matrix, $R_{\rm pp}(\theta,y)$ is reflectivity equation, $l(\theta)*R_{\rm pp}(\theta,y)$ is the forward operator linking model parameter and seismic data, and r is the random noise in the input data.

Within the Bayesian framework, the posterior pdf is constructed by the prior function of model parameters and the likelihood equation (Alemie and Sacchi, 2011; Li et al., 2022):

$$p(y|D(\theta)) \propto p(y) \cdot p(D(\theta)|y),$$
 (4)

where p(y) denotes prior probability of the inverted parameters, given by log data and geological information. $p(D(\theta)|y)$ denotes the likelihood probability associated with the model parameters and seismic data.

The inverted parameters are assumed to follow the mixed Gaussian distribution and random noise adheres to the Gaussian distribution (Li et al., 2022; Zuo et al., 2023), the posterior pdf is simplified to

$$p(y|D(\theta)) = \sum_{n=1}^{N} \lambda_n G\left(y; \mu_y^n, \sum_y^n\right) \cdot G\left(D(\theta)\right) - l(\theta) * R_{pp}(\theta, y), 0, \sum_e\right), \tag{5}$$

where N denotes the quantity of model parameters, λ_n refers to the weight assigned to each parameter within the Gaussian distribution, μ_y^n and \sum_y^n represent the mean and the covariance matrix of model parameters, and \sum_e denotes the noise covariance.

The inherent correlation among model parameters often leads to highly correlated random samples generated by the MCMC algorithms during sampling. Moreover, the conventional MCMC algorithm relies on random sampling from known pdf, such as the Gaussian and Cauchy distribution. The reliance restricts the ability to simulate random samples that align more closely with the target distribution. To address these limitations, the IADR-Gibbs sampling algorithm is proposed. The innovative approach constructs the proposal distribution utilizing a non-parametric distribution and employs support points for the adaptive updating of the proposal distribution. The novel algorithm significantly diminishes the constraints imposed by the known parameter distribution on random simulations. Furthermore, the algorithm incorporates a delayed rejection strategy, which reconsiders rejected samples with a specified probability, thereby enhancing the acceptance rate of random samples. The detailed workflow of the IADR-Gibbs algorithm is outlined below.

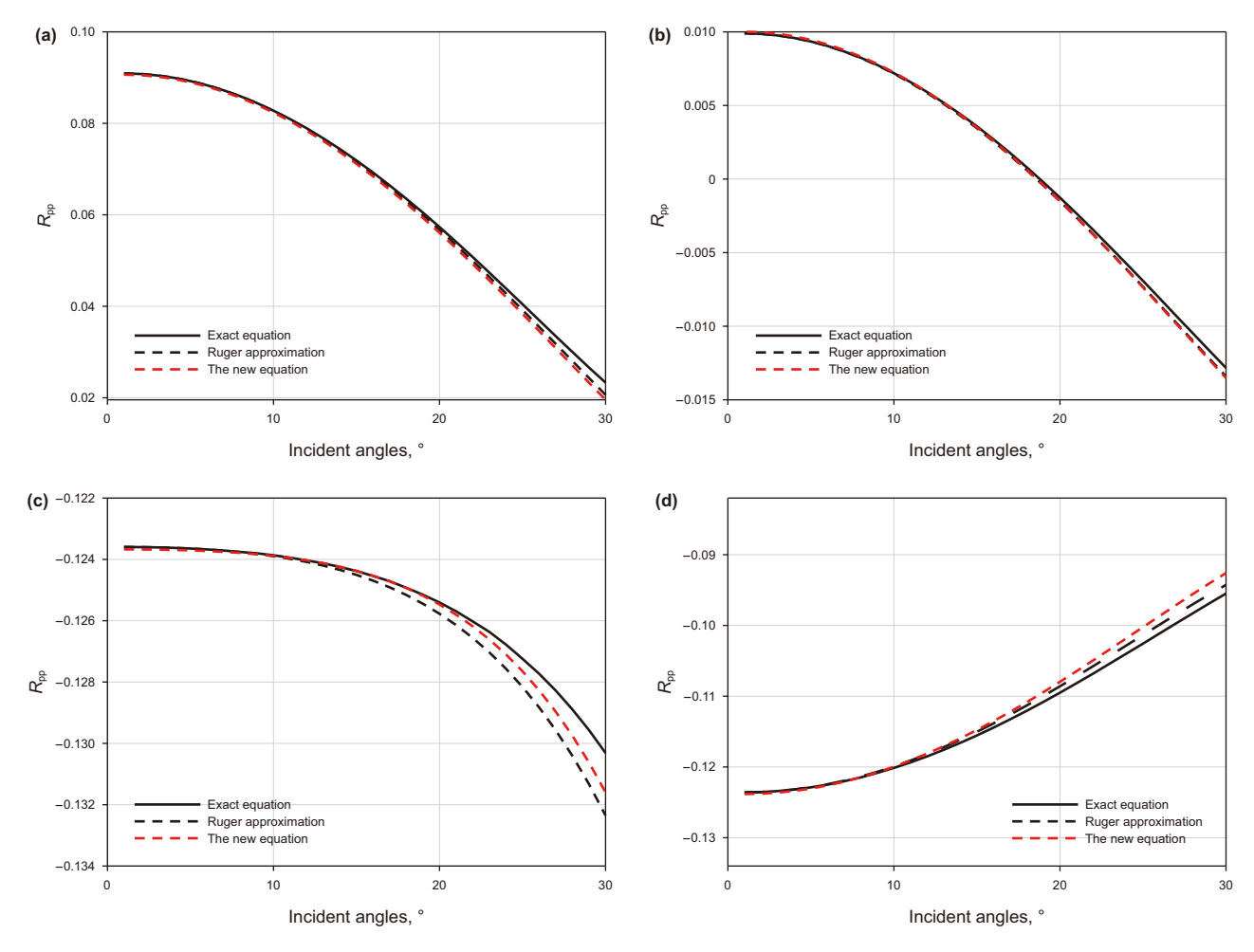


Fig. 1. PP-wave reflection coefficient of the exact VTI equation (black line), the Ruger approximation equation (black dotted line) and the new equation (red dotted line) for different AVO classes: (a) class I, (b) class II, (c) class III, (d) class IV.

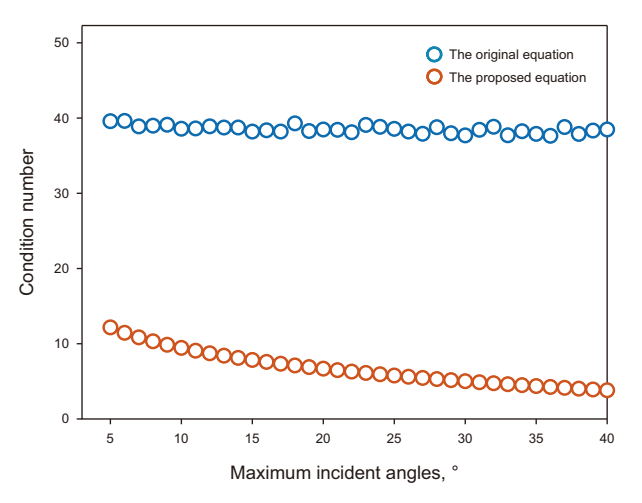


Fig. 2. Comparison of the condition number of the proposed equation (red dots) with that of the original equation (blue dots).

Firstly, set the initial parameters, the iteration number is T, the original inversion parameters represent $y^{(0)} = \{y_1^{(0)}, y_2^{(0)},, y_L^{(0)}\}$, where L represents the amount of model parameters.

As delineated by the Gibbs algorithm, the posterior pdf $P(y_l^{(t)})$ of the inverted parameters is defined as:

$$P(y_l^{(t)}) \propto p(y_l|y_{1:(l-1)}^{(t)}, y_{(l+1):(L)}^{(t-1)}, D(\theta)), \tag{6}$$

where the superscript t refers to the current iteration number, the subscript l represents the model parameter of the current sampling, $y_l^{(t)}$ is the l th parameter of t th iteration, $p(y_l | y_{1:(l-1)}^{(t)}, y_{(l+1):(L)}^{(t-1)}, D(\theta))$ refers to the conditional probability between the seismic data and other model parameters $y_{1:(l-1)}^{(t)}, y_{(l+1):(L)}^{(t-1)}$ and the current sampling parameter $y_l^{(t)}$.

Secondly, the initial support point of *t* th iteration is given as:

$$S_{y_l}^{(t)} = \left\{ m_{l(1)}, m_{l(2)}, ..., m_{l(k)} \right\}, \tag{7}$$

where k is the number of support points, which is gradually increasing, expressed as $m_{l(1)} < m_{l(2)} < ,..., < m_{l(k)}$. Support points refer to a discrete set of points used to construct the envelope function. The envelope function serves as an upper bound for the logarithmic density function of the posterior distribution, and it is dynamically adjusted using the support points. The initial support points are determined by the prior distribution of the model parameters and are updated whenever a candidate sample is rejected. The envelope function is continuously optimized to better approximate the posterior distribution.

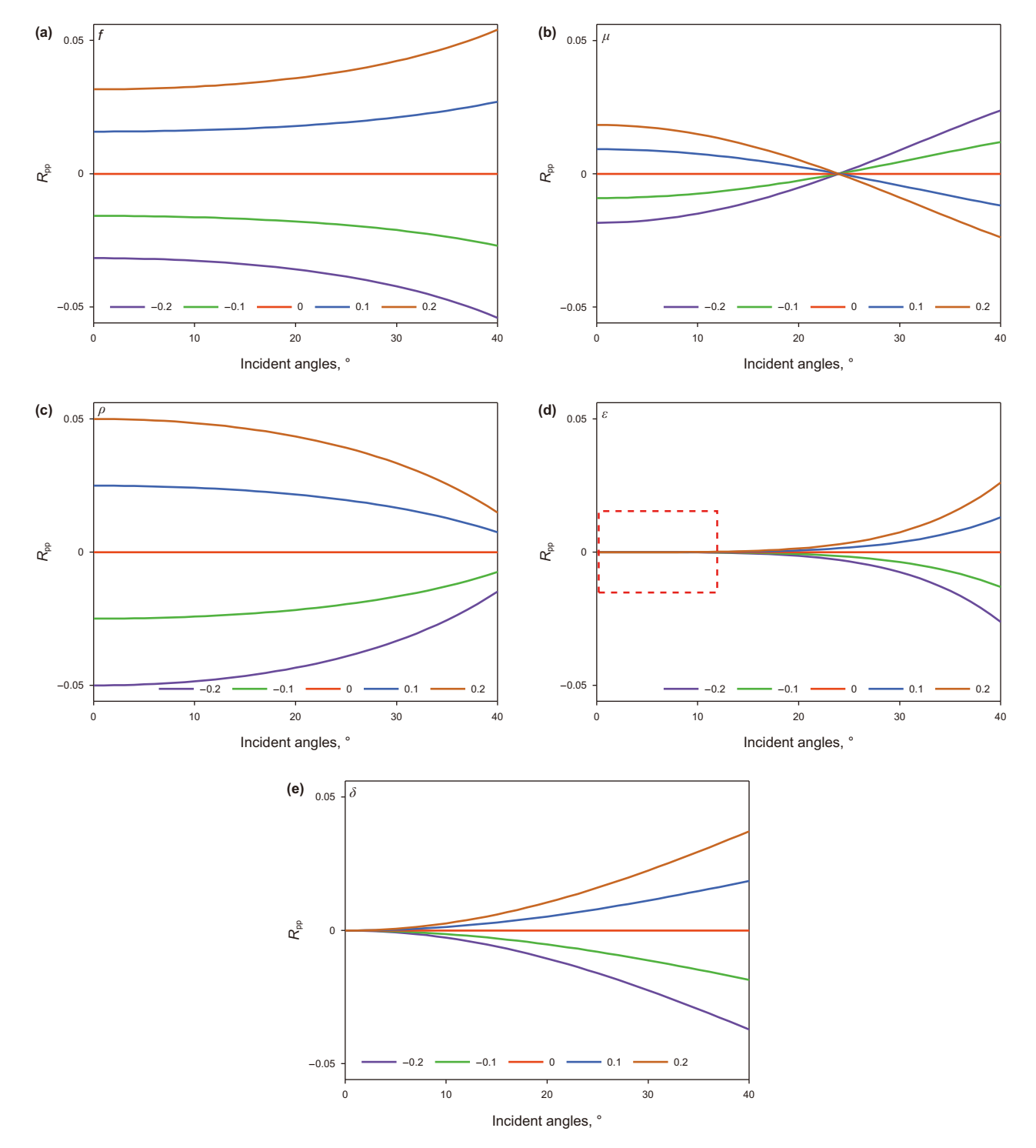
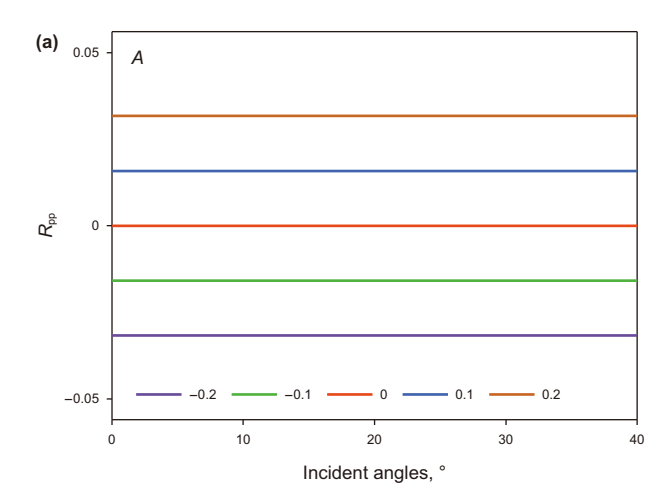
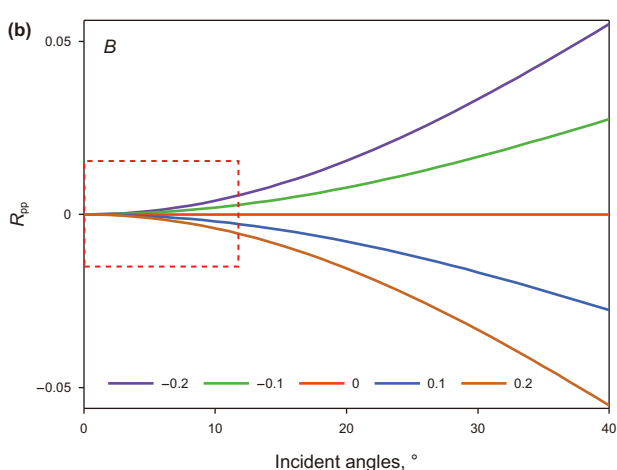


Fig. 3. Effects of changes in the **(a)** fluid term, **(b)** shear modulus, **(c)** density, **(d)** Thomsen anisotropy parameter ε , and **(e)** Thomsen anisotropy parameter δ on PP-wave reflection coefficient. Fig. 3(a) shows the reflection coefficient when only $\frac{\Delta f}{f}$ varies from -0.2 to 0.2, while other parameters remain zero, and Fig. 3(b)–(e) show reflection coefficients when only $\frac{\Delta \mu}{f}$, $\frac{\Delta \rho}{\rho}$, $\Delta \varepsilon$, and $\Delta \delta$ vary from -0.2 to 0.2, respectively.

The introduction of support points can realize the adaptive update of the proposal distribution. In the IADR algorithm, the proposal distribution of the attribute parameter [A,B,C] adopts a non-parametric distribution, which is constructed by a linear piecewise function shown in Fig. 6 in conjunction with support points:

$$Q_{y_{l}}^{(t)}\left(m\middle|S_{y_{l}}^{(t)}\right) = \begin{cases} F_{0}(m), m \in \left(0, m_{l(1)}\right] \\ F_{\nu,\nu+1}(m), m \in \left(m_{l(\nu)}, m_{l(\nu+1)}\right], \\ F_{k}(m), m \in \left(m_{l(k)}, +\infty\right] \end{cases}$$
(8)





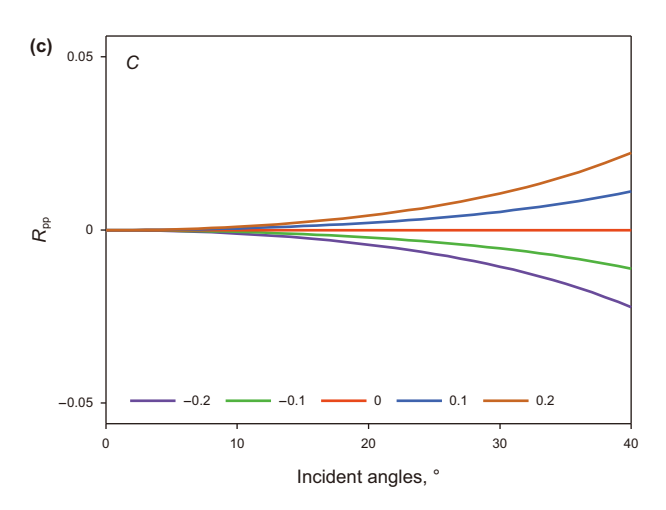


Fig. 4. Effects of changes in the **(a)** A, **(b)** B, and **(c)** C on PP-wave reflection coefficient. Fig. 4(a) shows the reflection coefficient when only $\ln \frac{|A|}{|A|}$ varies from -0.2 to 0.2, while other parameters remain zero, and Fig. 4(b) and (c) show reflection coefficients when only $\ln \frac{|B|}{|B|}$, and $\ln \frac{|C|}{|C|}$ vary from -0.2 to 0.2, respectively.

where the proposal distribution $Q_{y_l}^{(t)}(m | S_{y_l}^{(t)})$ is segmented into three intervals, $m \in (0, m_{l(1)}]$ and $m \in (m_{l(k)}, +\infty]$ delineate the start and finish of $Q_{y_l}^{(t)}(m | S_{y_l}^{(t)})$, and $m \in (m_{l(v)}, m_{l(v+1)}]$ is the central interval. $F_0(m)$ and $F_k(m)$ correspond to the exponential components of the piecewise linear function, $F_0(m)$ denotes $\exp(w_0(m))$, $w_0(x)$ is defined as the linear function connecting $(m_{l(1)}, \log(P(m_{l(1)}))), (m_{l(2)}, \log(P(m_{l(1)})))$

 $\log(P(m_{l(1)}))$). Likewise, $F_k(m)$ denotes $\exp(w_k(m))$, $w_k(m)$ is characterized as the linear function that unites the support points $(m_{l(k)}, \log(P(m_{l(k)})))$, $(m_{l(k+1)}, \log(P(m_{l(k+1)})))$. $F_{\nu,\nu+1}(m)$ represents the straight line that links $(m_{l(\nu)}, P(m_{l(\nu)}))$, $(m_{l(\nu+1)}, P(m_{l(\nu+1)}))$.

Then, the initial m^0 sample point and the current sample point m' are randomly simulated from the proposal distribution:

$$[m^0, m'] \sim Q_{y_l}^{(t)}(m|S_{y_l}^{(t)}).$$
 (9)

The current acceptance probability $\alpha(m^0|m')$ is defined as:

$$\alpha^{1}\left(m^{0}\middle|m'\right) = \min\left[1, \frac{P(m^{0})\min\left(P(m'), Q_{y_{l}}^{(t)}\left(m'\middle|S_{y_{l}}^{(t)}\right)\right)}{P(m')\min\left(P(m^{0}), Q_{y_{l}}^{(t)}\left(m^{0}\middle|S_{y_{l}}^{(t)}\right)\right)}\right]. \quad (10)$$

Generating a random number r^1 from a uniform distribution U(0,1), if $r^1 \leq \alpha^1(m^0|m')$, then $y_l^{(t)} = m', z = m^0$. z is defined as the sample points that are finally rejected. If $r^1 > \alpha^1(m^0|m')$, the newly generated sample point is rejected, then $y_l^{(t)^*} = m^0, z^* = m', y_l^{(t)^*} = m^0, z^* = m', y_l^{(t)^*}$ and z^* represent the intermediate variables of the rejected sample points, which are involved in the subsequent phase of the acceptance and rejection process. The process for selecting model parameters can be articulated as follows:

$$\begin{cases} y_{l}^{(t)} = m', z = m^{0}, r^{1} \leq \alpha^{1} \left(m^{0} \middle| m' \right), \\ y_{l}^{(t)^{*}} = m^{0}, z^{*} = m', r^{1} > \alpha^{1} \left(m^{0} \middle| m' \right). \end{cases}$$
(11)

Furthermore, the rejected samples are reselected and the support points are updated based on the DR strategy. The random numbers r^2 is generated from a uniform distribution U(0, 1), $r^2 \sim U(0, 1)$. If $r^2 > \alpha^2$, $\alpha^2 = Q_{y_l}^{(t)}(z^* \big| S_{y_l}^{(t)})/P(z^*)$, $y_l^{(t)} = y_l^{(t)^*}, z = z^*$, $S_{y_l}^{(t+1)} = S_{y_l}^{(t)} \cup \{z\}$, otherwise, $y_l^{(t)} = z^*, z = y_l^{(t)^*}, S_{y_l}^{(t+1)} = S_{y_l}^{(t)}$. These updated support points shown in Fig. 7 are then utilized in the adaptive refinement of the proposed distribution during the subsequent iteration. The methodology for constructing and reselecting the model parameters can be delineated as follows:

$$S_{y_l}^{(t+1)} = \begin{cases} S_{y_l}^{(t)} \cup \{z\}, r^2 > \alpha^2, \\ S_{y_l}^{(t)}, r^2 \le \alpha^2, \end{cases}$$
 (12)

$$\begin{cases} y_l^{(t)} = z^*, z = y_l^{(t)^*}, r^2 \le \alpha^2, \\ y_l^{(t)} = y_l^{(t)^*}, z = z^*, r^2 > \alpha^2. \end{cases}$$
(13)

Integrating the IADR algorithm with Gibbs sampling enhances the acceptance probability and reduces the correlation among random sampling points in the MCMC algorithm. The approach avoids the limitation of the known distribution of fixed parameters on sampling randomness. Initially, the Gibbs algorithm facilitates the generation of relatively independent sample points during random sampling. Subsequently, the DR strategy conducts a secondary selection for sample points previously rejected and updates the support points for rejected candidates. The updated support points establish a new proposal distribution using a linear piecewise function, enabling the non-parametric construction and independent adaptive update of the proposal distribution. With continuous iterations, the proposal distribution eventually converges to the posterior pdf of the model parameters. The flowchart of the algorithm is depicted in Fig. 8.

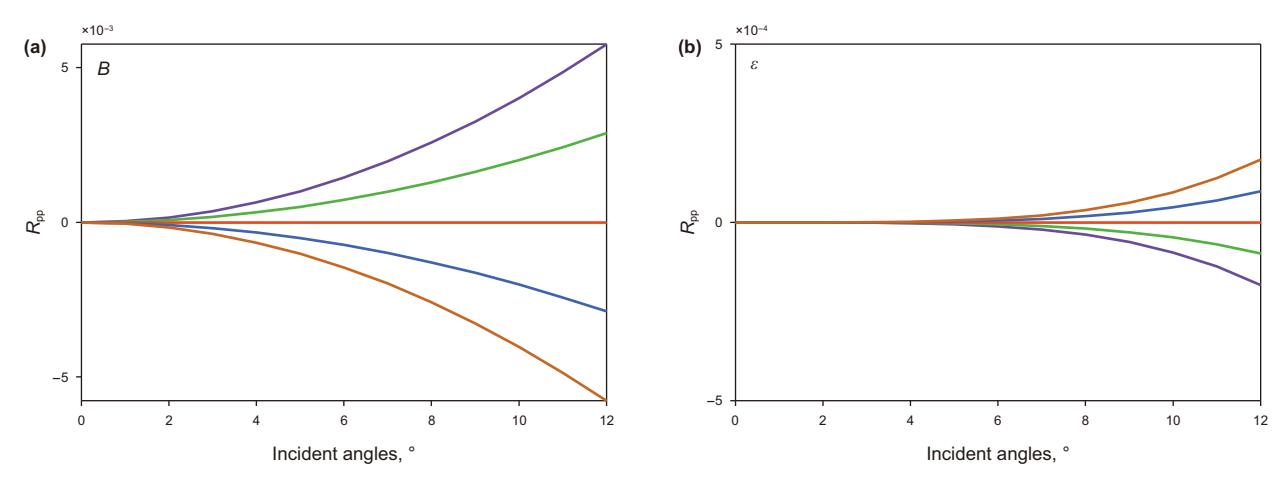


Fig. 5. Effects of changes in the (a) B and (b) Thomsen anisotropy parameter ε on PP-wave reflection coefficient.

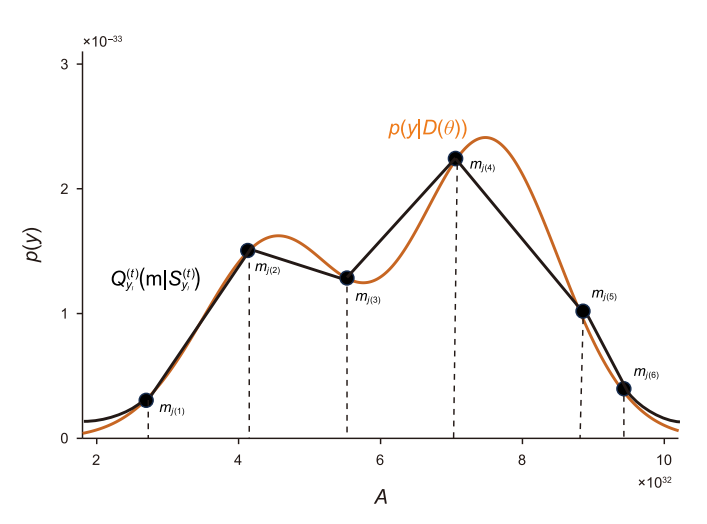


Fig. 6. Piecewise linear function of proposal distribution construction.

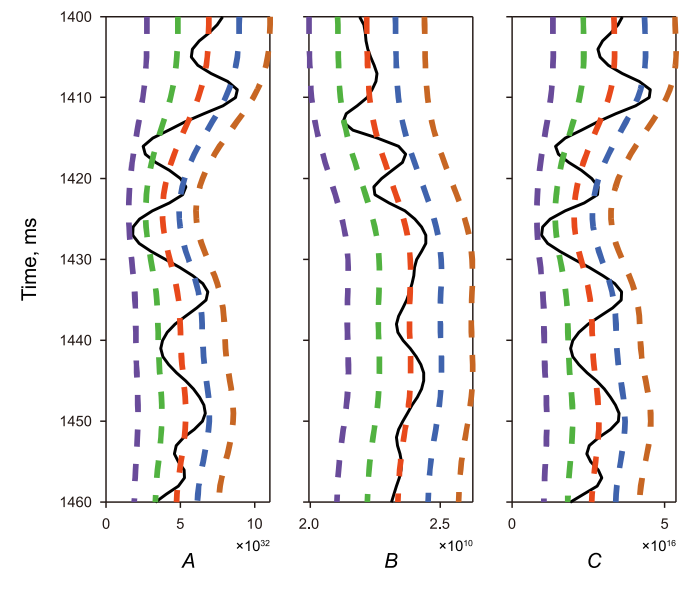


Fig. 7. Theoretical support points of parameters A, B, and C.

3. Numerical example

3.1. Synthetic case

The inversion method proposed above is applied to a shale gas exploration area. The original logging data includes P-wave velocity, S-wave velocity, density, and Thomsen anisotropy parameters, as illustrated in Fig. 9. Fig. 10(a) presents the synthetic seismic gathers without noise. Subsequently, random noise following a Gaussian distribution is added. The synthetic seismic gathers for signal-to-noise ratio (SNR) of 10 and 5 are shown in Fig. 10(b) and (c), respectively. SNR represents the relative ratio of the amplitude of the effective signal to the noise. Since the order of magnitudes between inverted parameters are different, leading to the estimation errors. In this study, fluid term and shear modulus, computed by the P-wave velocity, S-wave velocity, and density, are first normalized. Subsequently, anisotropy parameters are normalized. Finally, combined parameters A, B, and C, calculated from fluid term, shear modulus, density, and anisotropy parameters, are also normalized. Fig. 11(a)–(c) display the model test results for without noise, SNR = 10 and SNR = 5, respectively. The red curve denotes the inversion result, the green curve represents the initial model, the blue curve represents the original well data, and the grey dotted line indicates the 95% confidence interval, reflecting the uncertainty of the estimated results in probabilistic inversion. In the noise-free case, the inversion results of the three combined parameters, A, B, and C align with the well data. The uncertainty of the combined parameter *B* is the smallest, indicating that *B* contributes more significantly to the new equation, which corresponds to the above analysis results of the new equation. Fig. 11(b)-(c) demonstrate that the estimated results closely align with the logging curve even with the addition of random noise to the synthetic seismic gathers. The model test results validate the accuracy and noise resistance of the proposed inversion method. The condition number of the coefficient matrix in the new equation is low, stabilizing the equation and provides a certain degree of noise resistance. In combination with the IADR-Gibbs algorithm, the stable probabilistic nonlinear inversion results are finally predicted.

After obtaining the stable inversion results for the combination parameters, the prediction results for the fluid term, shear modulus, density, and Thomsen anisotropy parameter can be derived through algebraic operations. First, the shear modulus calculated using the well data (blue curve) and the estimated result

Y.-H. Zuo, Z.-Y. Zong, X.-Y. Yin et al. Petroleum Science 22 (2025) 3565–3582

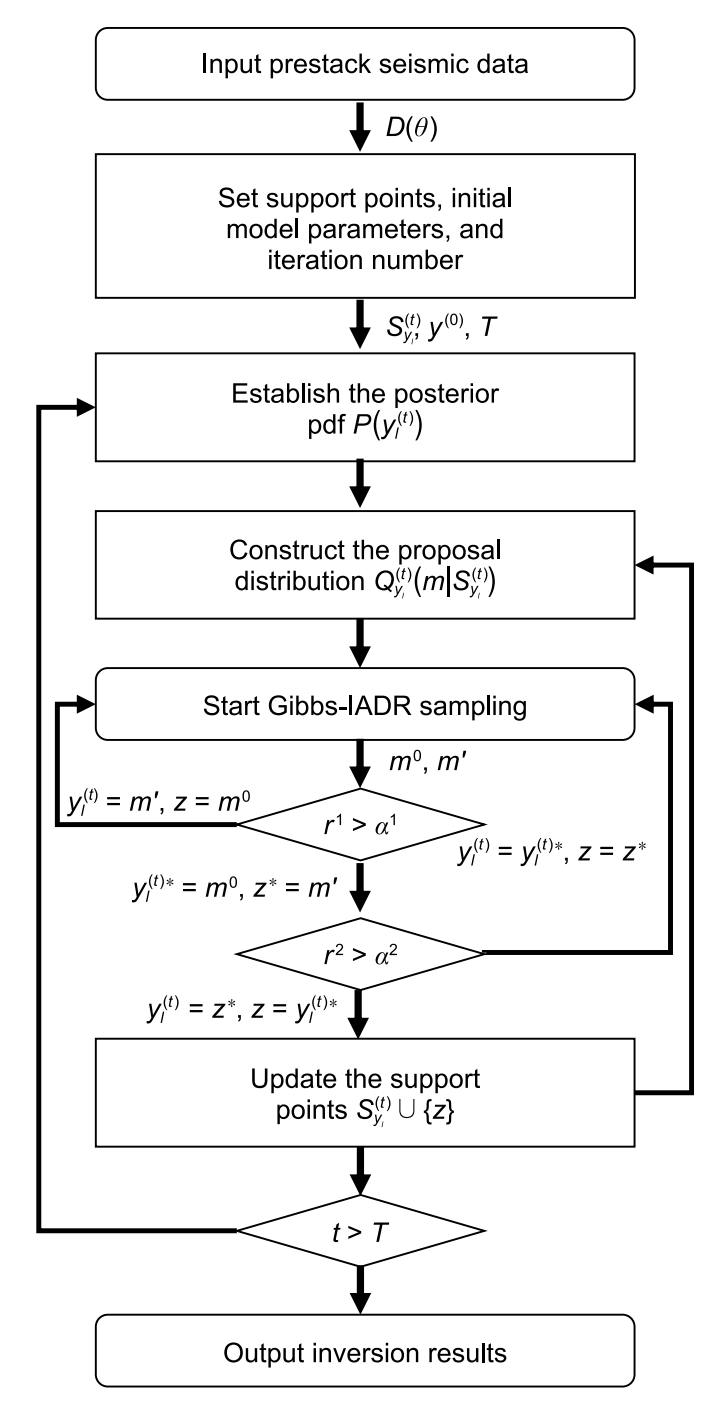


Fig. 8. The workflow of the IADR-Gibbs algorithm.

of the combination parameter B (red curve) are compared, as shown in Fig. 12(b). The difference between the two is minimal, indicating that the inversion result of B can be approximately characterized as the inversion result of the shear modulus. The error in B impacts the accuracy of the shear modulus. Next, the fluid factor can be obtained by calculating the combination parameter A, shear modulus, and density, according to $f = A / \left(\mu^{\frac{k_2}{k_1}} \rho^{\frac{1}{k_1}} \right)$. The errors in A and B impact the accuracy of the fluid factor. Since the sensitivity of small-angle seismic data to anisotropy is less than that of large-angle seismic data, we assume that the density changes minimally at the junction of the elastic interface and the density

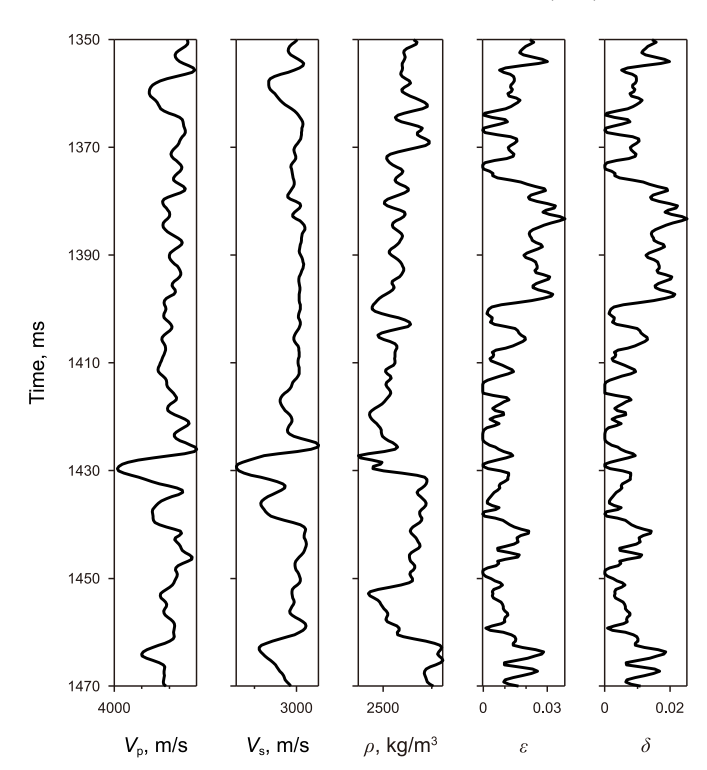


Fig. 9. Well curves for the synthetic case test.

can be estimated based on small-angle seismic data combined with the isotropic AVO inversion method (Alkhalifah and Tsvankin, 1995; Zhang et al., 2019). Furthermore, according to the equation $\varepsilon = \frac{k_1}{2} \ln \left(C \rho^{\frac{2}{k_1}} / A \right)$, the Thomsen anisotropy parameter ε can be calculated from the combination parameters A, C, and density. The errors in A and C impact the accuracy of the ε . The prediction results for the fluid term, density, and Thomsen anisotropy parameter are shown in Fig. 12(a), (c), (d), where the red curve refers to the predicted result and the blue curve represents the well data. Relative errors between inversion results and logging-data of various SNRs are given in Table 2.

Furthermore, inversion results of *A*, *B*, and *C* without noise based on the IADR-MCMC algorithm (in blue) and the MCMC algorithm (in red) are displayed as Fig. 13. Relative error convergence curves of *A*, *B*, and *C* for the noise-free case are shown as Fig. 14. The inversion errors associated with the IADR-MCMC algorithm are smaller than that of the MCMC algorithm, verifying the superiority of the proposed algorithm.

3.2. Real case

To further demonstrate the reliability of the method in this paper, actual data application is carried out based on the azimuthal pre-stack seismic data of the shale working area in Fuling, which is located in the Sichuan Basin of China. The reservoir targeted in this study is located in the Lianggaoshan Formation, which is the gassaturated fracture reservoir. The prestack seismic data is processed by denoising and removing multiple waves. Fig. 15 presents the pre-stack seismic data with incident angles of 6°, 18°, and 30°, where the vertical and horizontal axes represent the time and common-depth-point (CDP) number of seismic data, respectively. The seismic data has been processed to remove noise and maintain amplitude. Fig. 16(a)—(c) show the estimated results for *A*, *B*, and *C*, respectively. In the area enclosed by the white dotted line, all three

Y.-H. Zuo, Z.-Y. Zong, X.-Y. Yin et al. Petroleum Science 22 (2025) 3565—3582

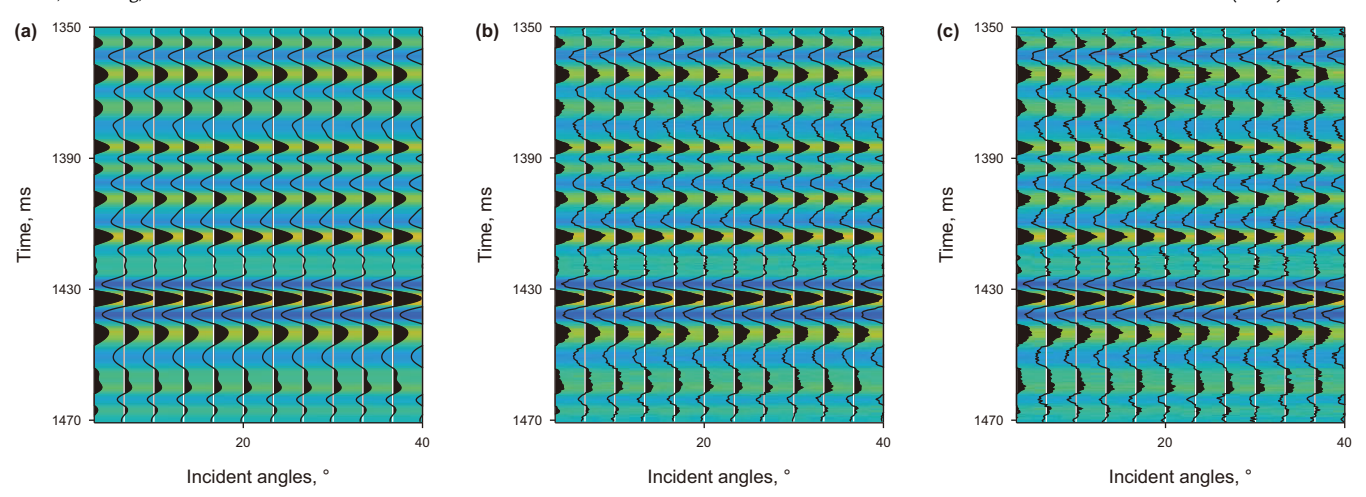


Fig. 10. Synthetic seismic gathers of (a) without noise, (b) SNR=10, (c) SNR=5.

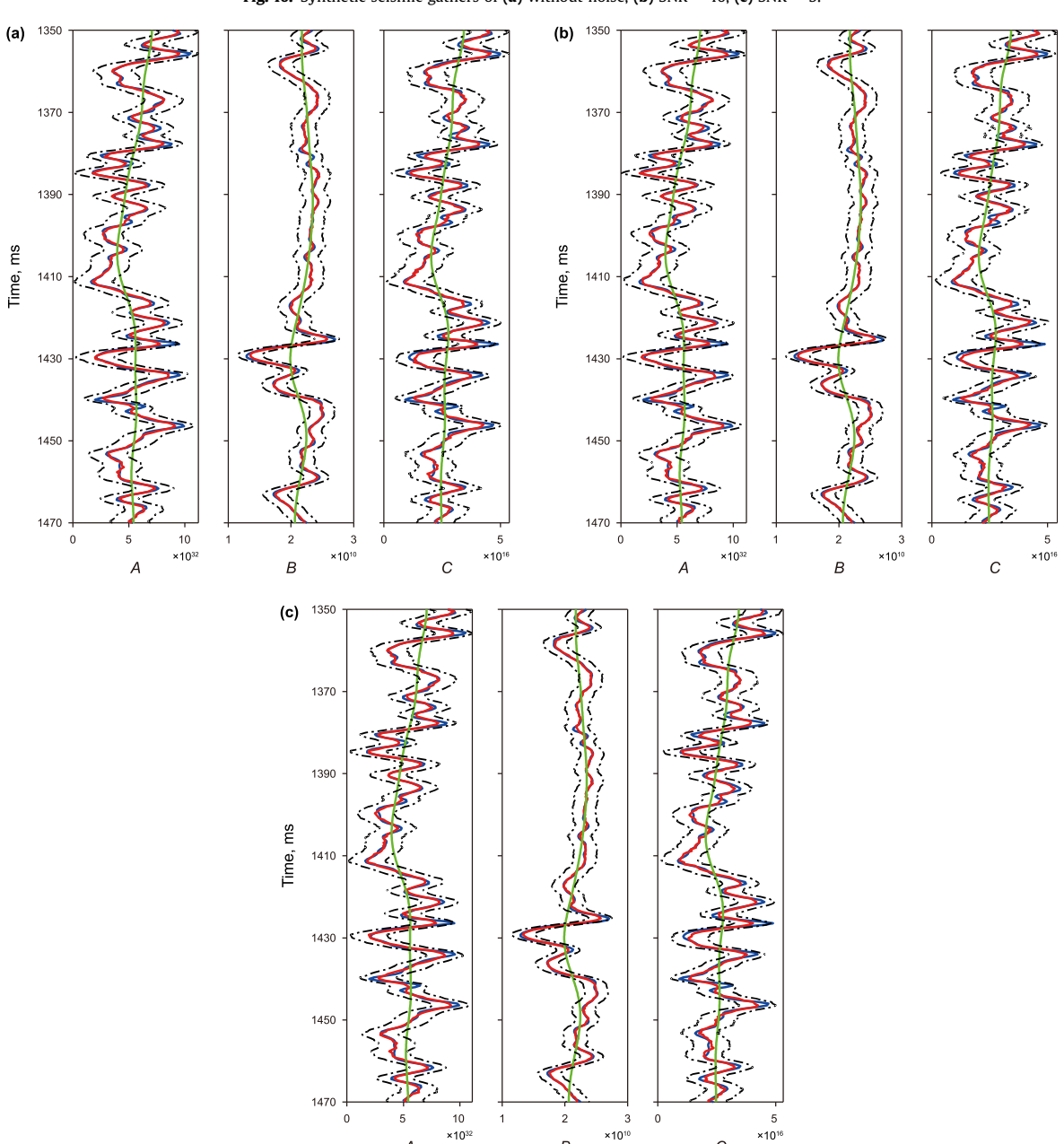


Fig. 11. Inversion results of A, B, and C: (a) without noise, (b) SNR = 10, (c) SNR = 5.

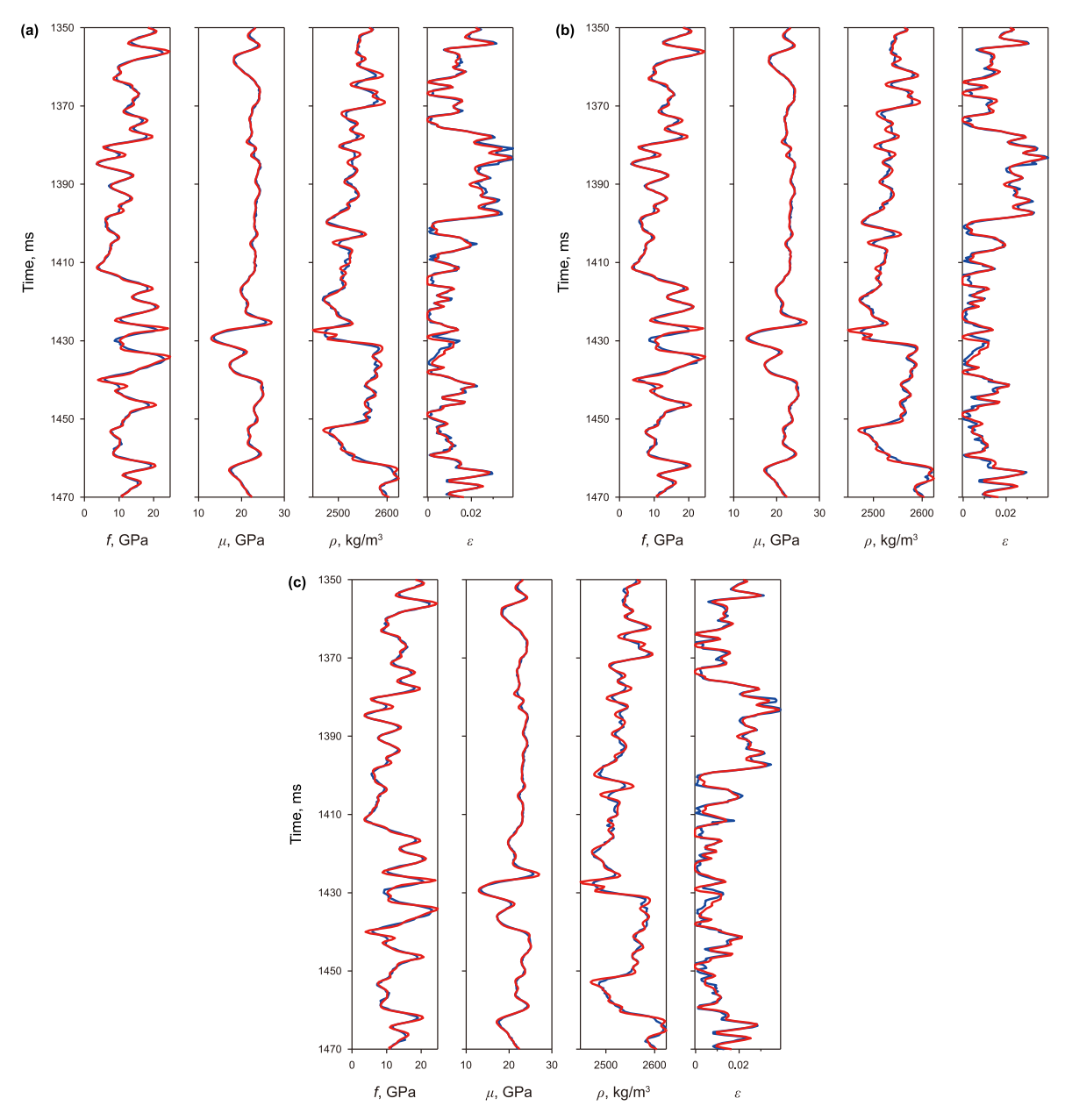


Fig. 12. Inversion results of the fluid term, shear modulus, density, and ε : (a) without noise, (b) SNR = 10, (c) SNR = 5.

 Table 2

 Relative errors between inversion results and logging-data of various SNRs.

SNR	Α	В	С	f, GPa	μ , GPa	ρ , kg/m ³	ε
Noise free 10 5	0.0179	0.0091	0.0218	0.0220 0.0291 0.0349	0.0105	0.0083	0.0520 0.0612 0.0698

attribute parameters, *A*, *B*, and *C*, exhibit abnormally low values, and the inversion results are consistent with the well-logging data. Comparison of estimated results and logging data of the 113rd seismic trace (CDP 113) are displayed in Fig. 17. Following the algebraic operations and assumptions described above, the prediction results for the fluid term, shear modulus, density, and Thomsen anisotropy parameter are shown in Fig. 18(a)–(d), respectively. The estimated results of four parameters align with the well curves, particularly in the area enclosed by the white

dotted line. The fluid term shows an abnormally low value, indicating that the reservoir segment is fluid-filled. Meanwhile, the Thomsen anisotropy parameter exhibits abnormally high values, signifying strong anisotropy characteristics in the reservoir segment. The application of actual data further validates the accuracy of the IADR-Gibbs inversion method proposed in this paper and its applicability in shale exploration areas.

4. Discussion

The stable and accurate inversion results of fluid factor and Thomsen anisotropy parameter are crucial for guiding reservoir fluid identification and evaluating engineering sweet spots, and are of great significance for the exploration and development of shale reservoirs.

First, an anisotropic reflectivity equation for VTI media containing three combined parameters, A, B, and C, is derived. The

Y.-H. Zuo, Z.-Y. Zong, X.-Y. Yin et al. Petroleum Science 22 (2025) 3565–3582

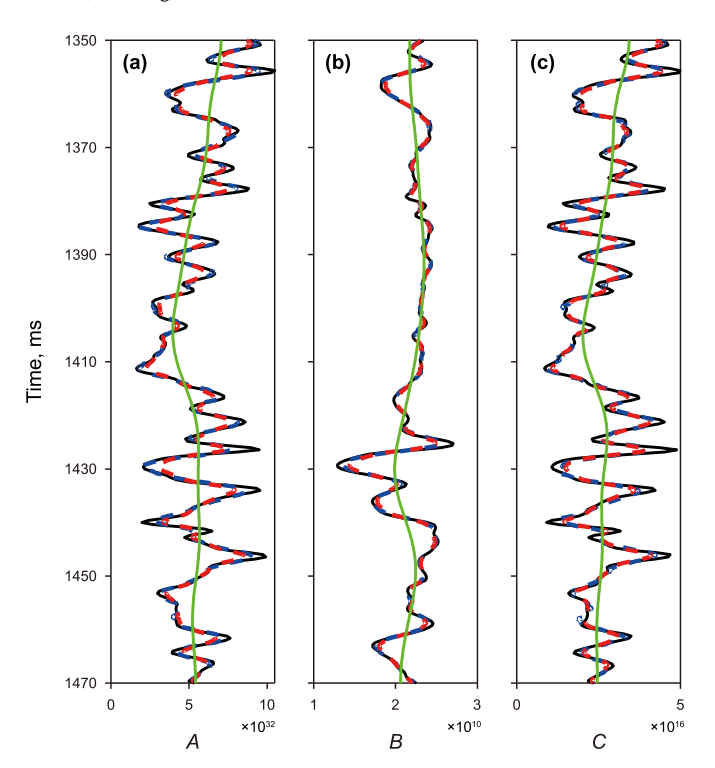


Fig. 13. Inversion results of **(a)** *A*, **(b)** *B*, and **(c)** *C* without noise based on the IADR-MCMC algorithm (in blue) and the MCMC algorithm (in red). The black curves represent the logging-data, and the green curves indicate the initial models.

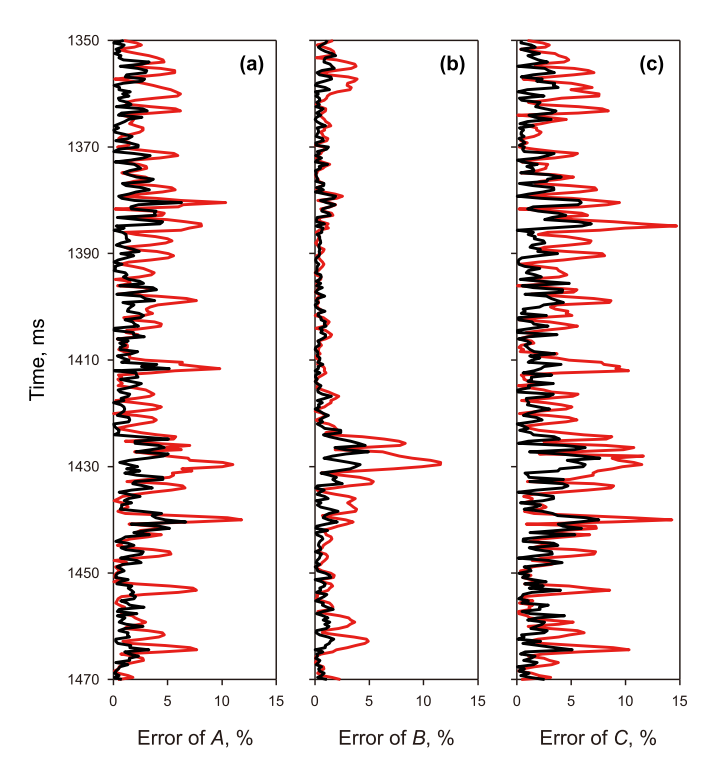
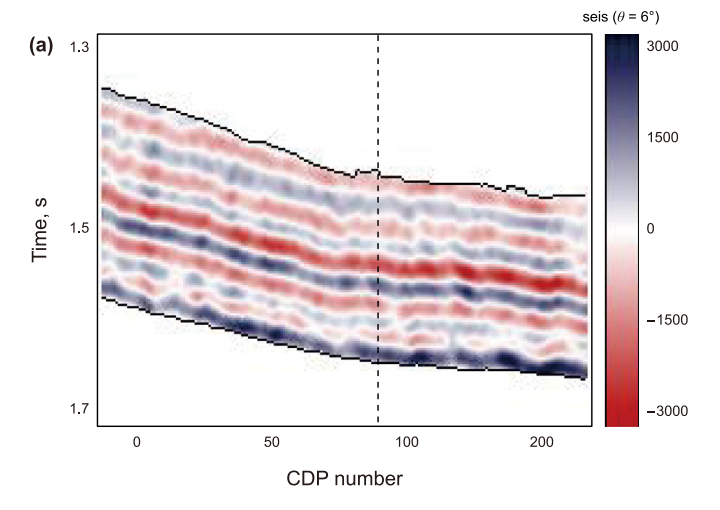
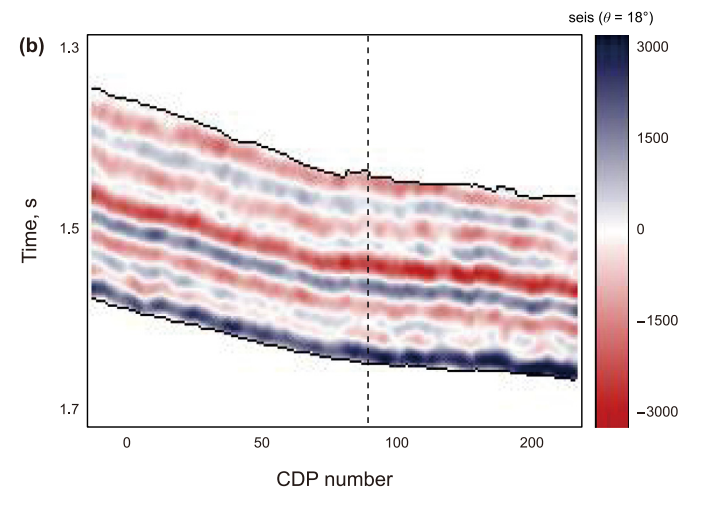


Fig. 14. Relative errors of **(a)** *A*, **(b)** *B*, and **(c)** *C* without noise based on the IADR-MCMC algorithm (in black) and the MCMC algorithm (in red).

method of parameter merging and equation rewriting reduces the number of inversion parameters in the new equation, thereby improving its stability. Given that the new equation is highly nonlinear and there is an implicit correlation between the model





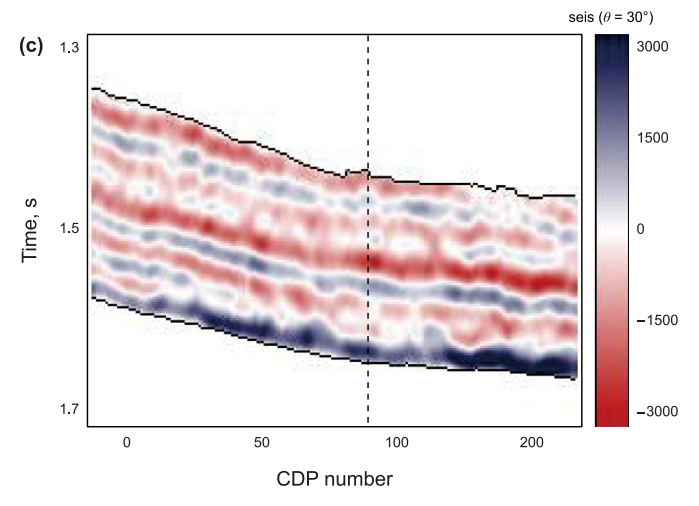
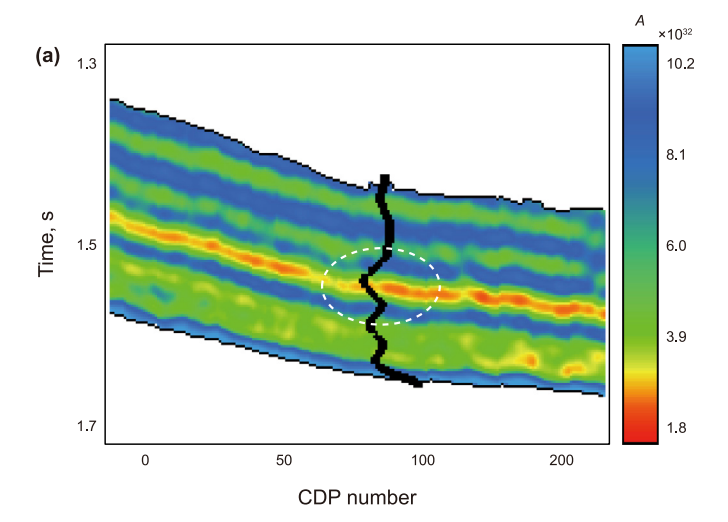
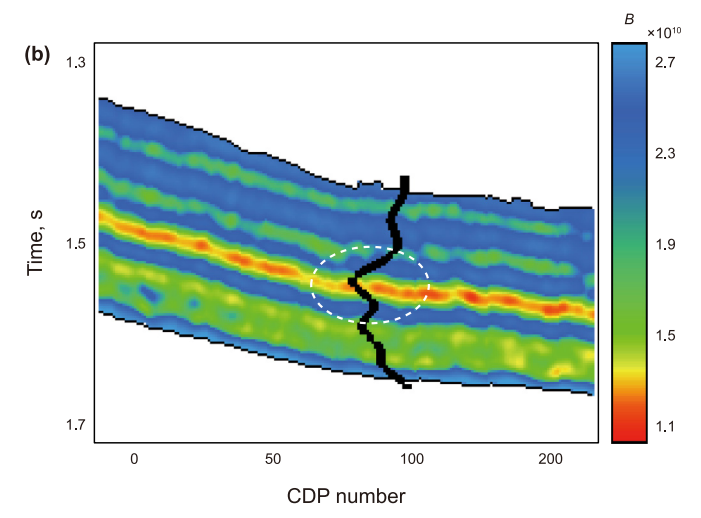


Fig. 15. Prestack seismic (seis) data from the shale exploration area with **(a)** incident angle 6° , **(b)** incident angle 18° , **(c)** incident angle 30° .

parameters, the IADR-Gibbs algorithm is proposed to achieve multi-parameter stable inversion. The algorithm randomly simulates relatively independent samples based on the Gibbs sampling criterion and introduces support points to construct the proposal distribution of the non-parametric function. Then, utilizing the delayed rejection strategy, the rejected samples are reselected with

Y.-H. Zuo, Z.-Y. Zong, X.-Y. Yin et al. Petroleum Science 22 (2025) 3565–3582





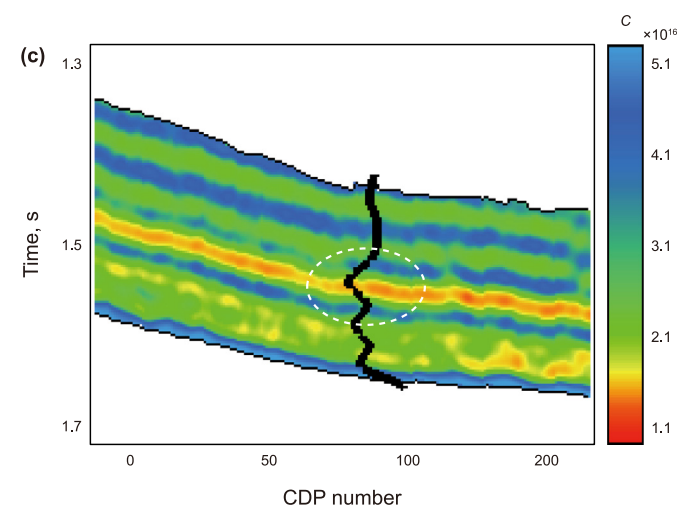


Fig. 16. Inversion results of **(a)** *A*, **(b)** *B*, **(c)** *C*.

a certain probability, achieving an adaptive update of the proposal distribution.

Second, the new equation, in comparison to the original equation, has fewer inversion parameters, and the condition number is

significantly reduced, which greatly enhances the stability of the equation. Additionally, the Thomsen anisotropy parameter ε that contribute less to the reflection coefficient are incorporated into the combined parameters A, B, and C, thereby increasing the parameters' contribution and improving the accuracy of the inversion. Zhang et al. (2019) proposed two strategies to predict the Thomsen anisotropy parameter ε by decoupling the predicted results of A. B. and C. The first strategy involves obtaining the inversion results of the independent parameters from the linear relationship between the combined parameters (such as attribute parameter A) and the independent parameters (such as P-wave velocity). Subsequently, the Thomsen anisotropy parameter ε is derived through algebraic operations based on its relationship with the combined parameters. The second strategy employs the isotropic AVO inversion method to obtain the P-wave velocity, S-wave velocity, and density. Then, it calculates the ε with the combined parameters. In this study, both strategies are adopted. According to the logging relationship between the combined parameter B and the shear modulus, the inversion result of B is approximately regarded as the inversion result of the shear modulus. The density is inverted using the isotropic AVO inversion method. The fluid term and Thomsen anisotropy parameter can be obtained through algebraic operations based on their relationship with the combined parameters A, B, and

Furthermore, the improved IADR-Gibbs algorithm, in comparison to the Gibbs sampling with adaptive independent sticky (AISM) MCMC algorithm (Zuo et al., 2024), introduce the DR strategy, which reselects the samples rejected in the previous state. Take parameter B as an example. Fig. 19(a)–(c) show the convergence process of B with 30 Markov chains using the IADR-Gibbs algorithm, Gibbs sampling with AISM algorithm, and traditional MCMC algorithm, respectively. It can be seen that when the Pearson correlation coefficient between the inversion result of B and the logging data reaches 0.916, the convergence iterations are 926, 1095, and 1165, respectively. The new algorithm converges faster than the Gibbs sampling with AISM algorithm, and traditional MCMC algorithm. Moreover, compared with the delayed rejection adaptive Metropolis (DRAM) MCMC algorithm (Zuo et al., 2023), the improved IADR-Gibbs algorithm employ the Gibbs sampling criterion instead of the Metropolis sampling criterion, which ensures the relative independence of random samples. In addition, the novel algorithm adopt the non-parametric distribution to construct the proposal distribution, which guarantees the randomness of sampling. Fig. 20(a)–(c) display the inversion results of B based on the IADR-Gibbs algorithm, DRAM-MCMC algorithm, and general MCMC algorithm, respectively. In the white dashed area, the inversion results of B using the new algorithm are in better agreement with the well logging data than using the DRAM-MCMC and general MCMC algorithm. And the lateral continuity of the inversion result is also improved by the IADR-Gibbs algorithm.

However, our study contains the following assumptions. First, in the process of stiffness matrix simplification and equation derivation, it is assumed that the anisotropy of the medium is weak, and the elastic parameters exhibit minimal variation at the elastic interface, so the equation is applicable to the inversion of reservoirs with small Thomsen anisotropy parameters and weak contrast interface. Second, the rock is saturated with fluid, and the stored fluid is a mixture of gas and water. Third, the inverted B can approximately characterize shear modulus under the premise of the weakly anisotropic VTI medium. Thus, the anisotropy parameter δ cannot be inverted using our method.

Besides, density is used to decouple fluid and anisotropy parameters from the inversion results of combined parameters A, B,

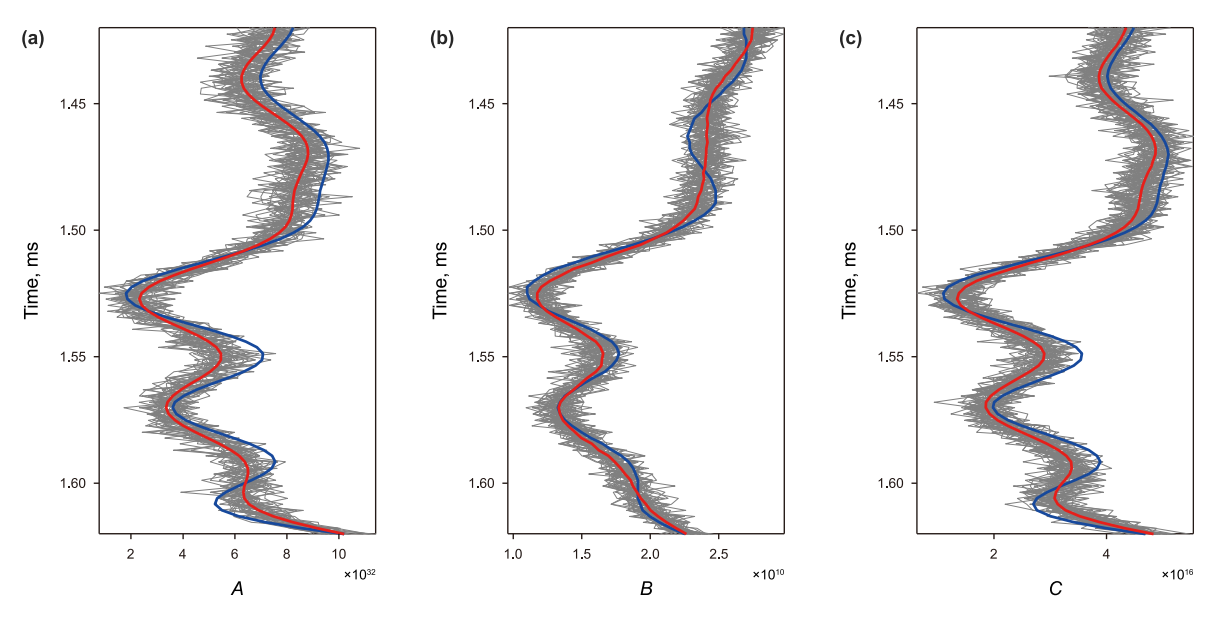


Fig. 17. Comparison of estimated results and logging data of the 113rd seismic trace (CDP 113). The blue curves indicate the true logging curves, the red curves indicate the predicted results, and the grey curves indicate the predicted results of 30 realizations. (a) A, (b) B, (c) C.

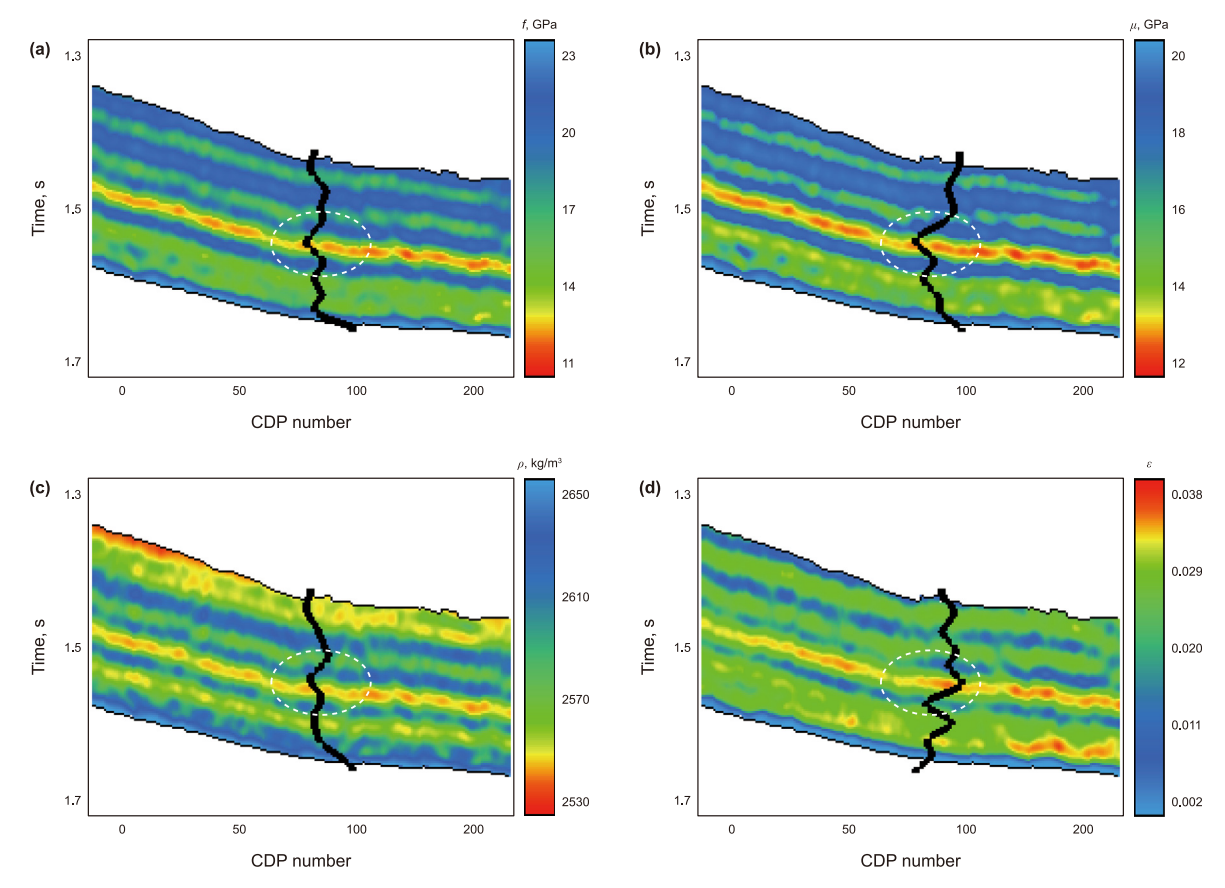


Fig. 18. Inversion results of the **(a)** fluid term, **(b)** shear modulus, **(c)** density, **(d)** ε .

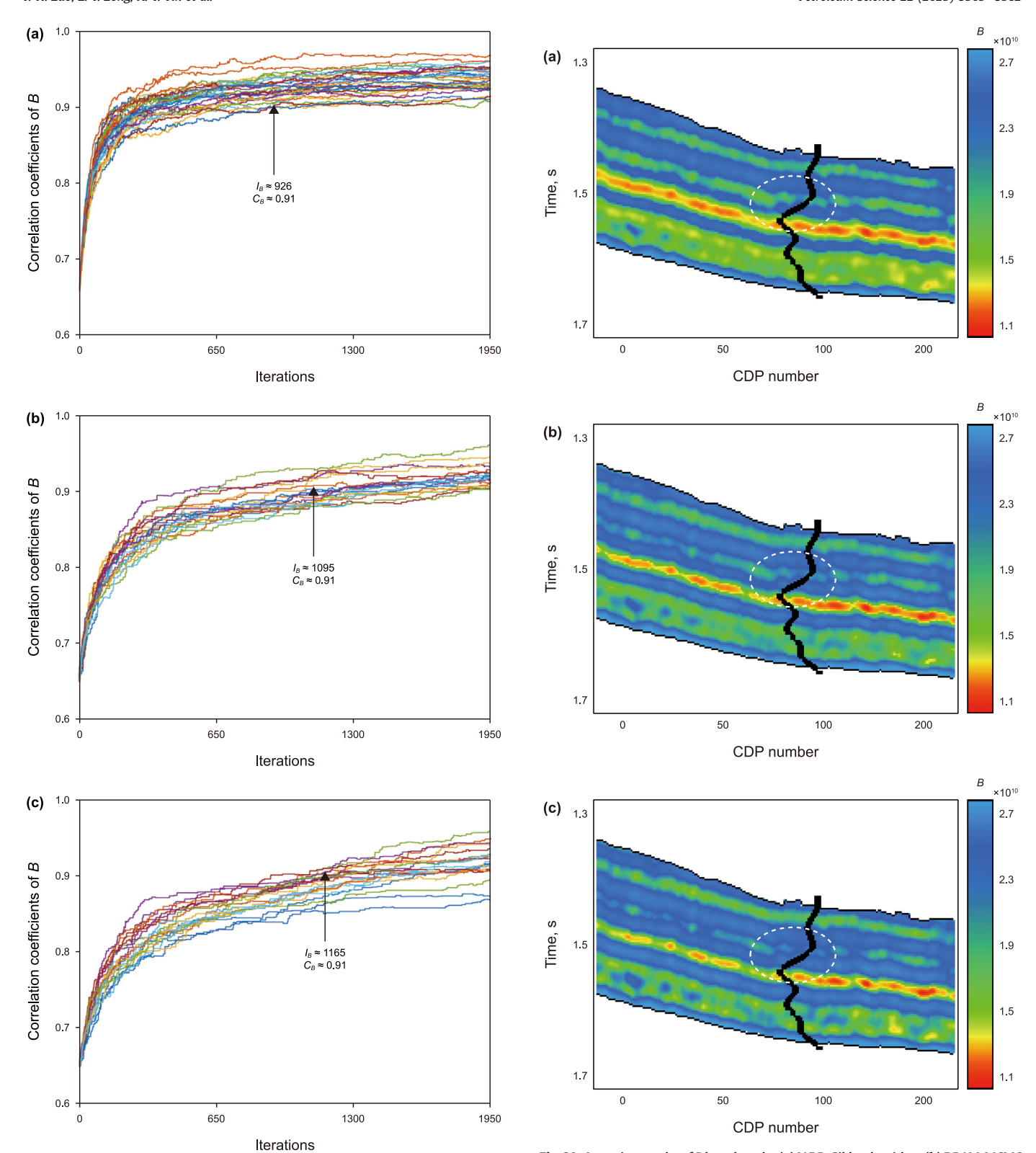


Fig. 19. Convergence process of B with 30 Markov chains using the **(a)** IADR-Gibbs algorithm, **(b)** Gibbs sampling with AISM algorithm, and **(c)** traditional MCMC algorithm. I_B and C_B represent iteration and Pearson correlation coefficient between the inversion result and logging data of B, respectively.

Fig. 20. Inversion results of B based on the **(a)** IADR-Gibbs algorithm, **(b)** DRAM-MCMC algorithm, and **(c)** general MCMC algorithm.

and *C*. However, the stability and accuracy of density inversion are influenced by its relatively small contribution to reflection coefficients and its strong correlation with other parameters. Additionally, the quality of seismic data significantly impacts the precision of density inversion. The large-angle seismic data is more prone to multiples and noise, requiring extensive preprocessing and corrections before inversion. In contrast, high-quality small-angle seismic data are better suited for density inversion. Therefore, we use the small-angle data to estimate density.

Finally, the reflectivity equation on the basis of the anisotropic medium assumption contains both isotropic and anisotropic parameter terms. Multiple model parameters reduce the stability of the equation and increase the uncertainty and decrease the accuracy of the inversion. Therefore, the equation rewriting method also applies to the derivation of anisotropic reflection coefficient equations based on the assumptions of the horizontal transverse isotropic medium, orthogonal transverse isotropic medium, and tilted transverse isotropic medium.

5. Conclusions

In this research, an innovative PP wave anisotropic reflectivity equation containing combined attribute parameters is derived using the equation rewriting method based on the VTI medium hypothesis. The estimated results of the attribute parameters *A*, *B*, and *C* can be used to obtain the prediction results for the fluid factor, shear modulus, density, and Thomsen anisotropy parameter through algebraic operations. The new equation reduces the coefficient matrix's condition number and incorporates the Thomsen anisotropy parameter, which has a lower contribution to the reflection coefficient, into the combined parameters to increase the prediction precision.

Additionally, the derived reflection coefficient equation retains strong nonlinear characteristics, and there is an implicit strong correlation between the combined parameters A, B, and C. To address this issue, the IADR-Gibbs probabilistic nonlinear inversion method is proposed. The method is based on the Gibbs sampling algorithm and randomly simulates relatively independent samples according to the conditional probability distribution between the model parameters. Furthermore, to overcome the high rejection probability of the traditional MCMC algorithm and the limitations of the randomness of the proposal distribution using known parameters such as the Gaussian distribution, support points are introduced to construct the proposal distribution using a linear piecewise function. During the random simulation process, the sample points rejected in the previous state are reselected with a certain probability based on the delayed rejection strategy. The rejected samples are finally added to the support points, and the proposal distribution of the non-parametric distribution is adaptively updated. Model testing and actual data application verify the accuracy of the equation derived in this paper, the proposed IADR-Gibbs inversion method, and their applicability to shale exploration areas.

CRediT authorship contribution statement

Ying-Hao Zuo: Writing — original draft. **Zhao-Yun Zong:** Supervision, Funding acquisition. **Xing-Yao Yin:** Investigation,

Conceptualization. **Kun Li:** Formal analysis, Data curation. **Ya-Ming Yang:** Validation, Methodology. **Si Wu:** Writing — review & editing.

Declaration of competing interest

The authors declare that they have no known competing financial interests or personal relationships that could have appeared to influence the work reported in this paper.

Acknowledgement

The authors cordially thank the sponsorship of the Key Technology for Geophysical Prediction of Ultra-Deep Carbonate Reservoirs (P24240), the National Natural Science Foundation of China (U24B2020), and the National Science and Technology Major Project of China for New Oil and Gas Exploration and Development (Grant No. 2024ZD1400102).

Appendix A

The stiffness matrix of VTI medium is expressed as:

$$\mathbf{C}_{\text{VTI}} = \begin{bmatrix} C_{11} & C_{12} & C_{13} & 0 & 0 & 0 \\ C_{12} & C_{11} & C_{13} & 0 & 0 & 0 \\ C_{13} & C_{13} & C_{33} & 0 & 0 & 0 \\ 0 & 0 & 0 & C_{55} & 0 & 0 \\ 0 & 0 & 0 & 0 & C_{55} & 0 \\ 0 & 0 & 0 & 0 & 0 & C_{66} \end{bmatrix}, \tag{A-1}$$

where $C_{12} = C_{11} - 2C_{66}$.

Operating under the premise of the weakly anisotropic medium, Thomsen (1986) streamline the formulation of each element within the stiffness matrix:

$$\begin{split} C_{11} &= \rho V_{p}^{\ 2}((1+2\varepsilon)) = M_{sat}(1+2\varepsilon), \\ C_{13} &= \rho V_{p}^{\ 2} \sqrt{F(F+2\delta)} - \rho V_{s}^{\ 2} = M_{sat} \sqrt{F(F+2\delta)} - \mu, \\ C_{33} &= \rho V_{p}^{\ 2} = M_{s}, \\ C_{55} &= \rho V_{s}^{\ 2} = \mu, \\ C_{66} &= \rho V_{s}^{\ 2}(1+2\gamma) = \mu(1+2\gamma), \\ F &= 1 - V_{p}^{\ 2} \Big/ V_{s}^{\ 2}, \end{split} \tag{A-2} \label{eq:A-2}$$

where V_p^2 and V_s^2 denote the P-wave and S-wave velocity propagating along the symmetry axis, ρ refers to the density of the medium, ε , δ , and γ are parameters represents the anisotropy strength of the VTI medium.

In the stiffness matrix component C_{13} , $\sqrt{F(F+2\delta)}$ cannot be directly decoupled, complicating the subsequent derivation of the reflection coefficient equation. To circumvent this complexity, Taylor's first-order approximation is employed to streamline the term, with the resulting simplified equation presented as Eq. (A-3). As depicted in Fig. 21, the simplified equation closely aligns with the original, exerting minimal impact on the component C_{13} .

$$\sqrt{F(F+2\delta)} \approx F + \delta.$$
 (A-3)

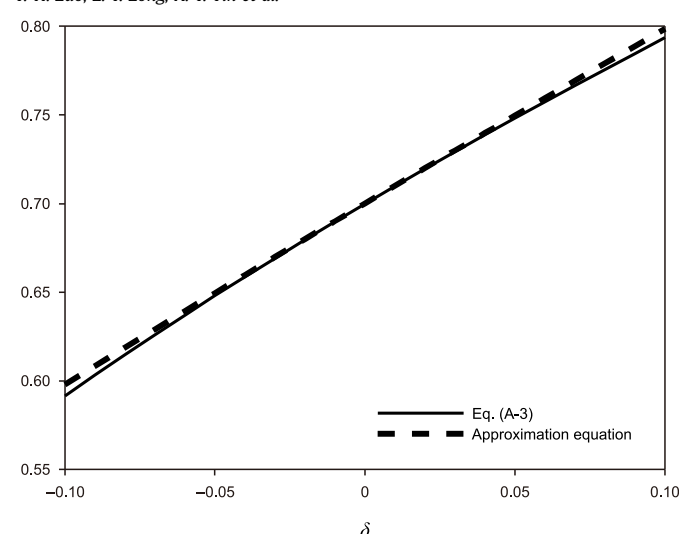


Fig. 21. Comparison of Eq. (A-3) and its approximation equation.

Then, C_{13} is simplified as:

$$C_{13} = \rho V_{\rm p}^{2} (F + \delta) - \rho V_{\rm s}^{2}.$$
 (A-4)

According to the definition of Russell et al. (2003), the fluid term *f* is given below:

$$f = (\rho V_{p}^{2})_{sat} - \alpha_{dry}^{2} (\rho V_{s}^{2})_{sat} = M_{sat} - \alpha_{dry}^{2} \mu$$

$$\alpha_{dry}^{2} = (V_{p}/V_{s})_{dry}^{2}, \alpha_{sat}^{2} = (V_{p}/V_{s})_{sat}^{2} = M_{sat}/\mu.$$
(A-5)

where the subscripts sat and dry denote saturated rock and dry rock, $M_{\rm sat}$ and μ represents P-wave modulus and shear modulus of the saturated rock, respectively. $\alpha_{\rm dry}^2$ and $\alpha_{\rm sat}^2$ can be obtained employing the method proposed by Chen and Zhang (2017).

Then, the stiffness matrix components in Eq. (A-1) are defined as:

$$\begin{split} C_{11} &= \left(f + \alpha_{\text{dry}}^2 \mu \right) (1 + 2\varepsilon) \\ C_{12} &= f + \left(\alpha_{\text{dry}}^2 - 2 \right) \mu + \left(f + \alpha_{\text{dry}}^2 \mu \right) 2\varepsilon - 4\mu \gamma \\ C_{13} &= f + \left(\alpha_{\text{dry}}^2 - 2 \right) \mu + \left(f + \alpha_{\text{dry}}^2 \mu \right) \delta \\ C_{33} &= f + \alpha_{\text{dry}}^2 \mu, \\ C_{55} &= \mu, \\ C_{66} &= \mu (1 + 2\gamma). \end{split} \tag{A-6}$$

The perturbation matrix of the stiffness parameters is:

Under the premise that the fluid term and shear modulus exhibit minimal variation at the elastic interface due to weak anisotropic media, the terms proportional to $\varepsilon \Delta f$, $\varepsilon \Delta \mu$, $\Delta \mu \gamma$, $\delta \Delta f$, and $\Delta \mu \delta$ are omitted and the matrix components are simplified to:

$$\begin{split} &\Delta C_{11} = \Delta f + \alpha_{\rm dry}^2 \Delta \mu + 2\Delta \varepsilon f + 2\alpha_{\rm dry}^2 \mu \Delta \varepsilon \\ &\Delta C_{12} = \Delta f + \left(\alpha_{\rm dry}^2 - 2\right) \Delta \mu + 2\Delta \varepsilon f + 2\alpha_{\rm dry}^2 \mu \Delta \varepsilon - 4\mu \Delta \gamma \\ &\Delta C_{13} = \Delta f + \left(\alpha_{\rm dry}^2 - 2\right) \Delta \mu + \Delta \delta f + \alpha_{\rm dry}^2 \mu \Delta \delta \\ &\Delta C_{33} = \Delta f + \alpha_{\rm dry}^2 \Delta \mu \\ &\Delta C_{55} = \Delta \mu \\ &\Delta C_{66} = \Delta \mu + 2\mu \Delta \gamma. \end{split} \tag{A-8}$$

Based on the scattering theory and Born approximation (Shaw and Sen, 2004), the PP wave reflection coefficient of VTI medium is defined as:

$$R_{\rm pp}(\theta,\varphi) = \frac{1}{4\rho\cos^2\theta} S(r_0),\tag{A-9}$$

where θ denotes the incident angle, $S(r_0)$ represents the scatter function which is expressed as:

$$S(r_0) = \Delta \rho \cos 2\theta + \Delta C \varsigma, \tag{A-10}$$

where $\Delta \rho$ is the perturbation of the density at the interface, ΔC is the perturbation matrix of the stiffness parameters derived above, ς is the function of slowness and polarization, which is defined as:

$$\begin{split} &\eta_{11} = \rho \cos^4 \varphi \sin^4 \theta \Big/ M_{\text{sat}}, \\ &\eta_{12} = \eta_{21} = \rho \sin^2 \varphi \cos^2 \varphi \sin^4 \theta \Big/ M_{\text{sat}}, \\ &\eta_{13} = \eta_{31} = \rho \cos^2 \varphi \sin^2 \theta \cos^2 \theta \Big/ M_{\text{sat}}, \\ &\eta_{22} = \rho \sin^4 \varphi \sin^4 \theta \Big/ M_{\text{sat}}, \\ &\eta_{23} = \eta_{32} = \rho \sin^2 \varphi \sin^2 \theta \cos^2 \theta \Big/ M_{\text{sat}}, \\ &\eta_{33} = \rho \cos^4 \varphi \Big/ M_{\text{sat}}, \\ &\eta_{44} = -4\rho \sin^2 \varphi \sin^2 \theta \cos^2 \theta \Big/ M_{\text{sat}}, \\ &\eta_{55} = -4\rho \cos^2 \varphi \sin^2 \theta \cos^2 \theta \Big/ M_{\text{sat}}, \\ &\eta_{66} = 4\rho \sin^2 \varphi \cos^2 \varphi \sin^4 \theta \Big/ M_{\text{sat}}. \end{split}$$

where φ represents the azimuth angle, which is 0° here. Combining Eqs. (A-8) to (A-11), the approximate VTI medium reflection coef-

$$\begin{split} &\Delta C_{11} = \Delta f + \alpha_{\rm dry}^2 \Delta \mu + 2\varepsilon \Delta f + 2\Delta \varepsilon f + 2\alpha_{\rm dry}^2 \varepsilon \Delta \mu + 2\alpha_{\rm dry}^2 \mu \Delta \varepsilon \\ &\Delta C_{12} = \Delta f + \left(\alpha_{\rm dry}^2 - 2\right) \Delta \mu + 2\varepsilon \Delta f + 2\Delta \varepsilon f + 2\alpha_{\rm dry}^2 \varepsilon \Delta \mu + 2\alpha_{\rm dry}^2 \mu \Delta \varepsilon - 4\Delta \mu \gamma - 4\mu \Delta \gamma \\ &\Delta C_{13} = \Delta f + \left(\alpha_{\rm dry}^2 - 2\right) \Delta \mu + \delta \Delta f + \Delta \delta f + \alpha_{\rm dry}^2 \mu \Delta \delta + \alpha_{\rm dry}^2 \Delta \mu \delta \\ &\Delta C_{33} = \Delta f + \alpha_{\rm dry}^2 \Delta \mu \\ &\Delta C_{55} = \Delta \mu \\ &\Delta C_{66} = \Delta \mu + 2\Delta \mu \gamma + 2\mu \Delta \gamma. \end{split} \tag{A-7}$$

 Δf , $\Delta \mu$, $\Delta \rho$, $\Delta \varepsilon$, and $\Delta \delta$ refer to the variation of fluid term, shear modulus, density, and Thomsen anisotropy parameter at the medium interface.

ficient equation including the fluid factor and anisotropic parameters is derived as follows:

$$R_{\rm pp}(\theta) = a(\theta) \frac{\Delta f}{f} + b(\theta) \frac{\Delta \mu}{\mu} + c(\theta) \frac{\Delta \rho}{\rho} + d(\theta) \Delta \varepsilon + e(\theta) \Delta \delta, \eqno(A-12)$$

$$\begin{split} a(\theta) &= \left(1 - \frac{\alpha_{\text{dry}}^2}{\alpha_{\text{sat}}^2}\right) \frac{\sec^2 \theta}{4}, \\ b(\theta) &= \left(\frac{\alpha_{\text{dry}}^2}{\alpha_{\text{sat}}^2} \frac{\sec^2 \theta}{4} - \frac{2}{\alpha_{\text{sat}}^2} \sin^2 \theta\right), \\ c(\theta) &= \left(\frac{1}{2} - \frac{\sec^2 \theta}{4}\right), \\ d(\theta) &= \frac{\sin^4 \theta}{2\cos^2 \theta}, \\ e(\theta) &= \frac{\sin^2 \theta}{2}. \end{split} \tag{A-13}$$

Letting
$$k_1 = 1 - \frac{\alpha_{\text{dry}}^2}{\alpha_{\text{tot}}^2}, k_2 = \frac{\alpha_{\text{dry}}^2}{\alpha_{\text{tot}}^2}, k_3 = \frac{2}{\alpha_{\text{tot}}^2}$$
, we can get:

$$\begin{split} a(\theta) &= k_1 \bigg(\frac{1}{4} + \frac{1}{4} tan^2 \; \theta \bigg), \\ b(\theta) &= \frac{1}{4} k_2 + \frac{1}{4} k_2 \; tan^2 \; \theta - k_3 \; sin^2 \; \theta, \\ c(\theta) &= \frac{1}{4} - \frac{1}{4} tan^2 \; \theta, \\ d(\theta) &= \frac{tan^2 \; \theta}{2} - \frac{sin^2 \; \theta}{2}, \\ e(\theta) &= \frac{sin^2 \; \theta}{2}. \end{split} \tag{A-14}$$

Rewriting Eq. (A-12), it can be expressed as:

$$\begin{split} A_1 &= \frac{1}{4} k_1 \left(\frac{\Delta f}{f} + \frac{k_2}{k_1} \frac{\Delta \mu}{\mu} + \frac{1}{k_1} \frac{\Delta \rho}{\rho} \right), \\ A_2 &= -k_3 \sin^2 \theta \left(\frac{\Delta \mu}{\mu} + \frac{1}{2k_3} \Delta \varepsilon - \frac{1}{2k_3} \Delta \delta \right), \\ A_3 &= \frac{1}{4} k_1 \tan^2 \theta \left(\frac{\Delta f}{f} + \frac{k_2}{k_1} \frac{\Delta \mu}{\mu} - \frac{1}{k_1} \frac{\Delta \rho}{\rho} + \frac{2}{k_1} \Delta \varepsilon \right). \end{split} \tag{A-15}$$

We introduce the approximate equation:

$$\frac{\Delta f}{f} \approx \ln\left(\frac{f_{i+1}}{f_i}\right), \frac{\Delta \mu}{\mu} \approx \ln\left(\frac{\mu_{i+1}}{\mu_i}\right), \frac{\Delta \rho}{\rho} \approx \ln\left(\frac{\rho_{i+1}}{\rho_i}\right). \tag{A-16}$$

The subscripts i+1 and i represent the (i+1)th layer and the ith layer, respectively.

Then, Eq. (A-12) is simplified to:

$$\begin{split} R_{\mathrm{pp}}(\theta) &= \frac{1}{4} k_{1} \ln \left[\frac{\left(f \mu^{\frac{k_{2}}{k_{1}}} \rho^{\frac{1}{k_{1}}} \right)_{i+1}}{\left(f \mu^{\frac{k_{2}}{k_{1}}} \rho^{\frac{1}{k_{1}}} \right)_{i}} \right] - k_{3} \sin^{2} \theta \ln \left[\frac{\left(\mu e^{\frac{1}{2k_{3}} \varepsilon - \frac{1}{2k_{3}} \delta} \right)_{i+1}}{\left(\mu e^{\frac{1}{2k_{3}} \varepsilon - \frac{1}{2k_{3}} \delta} \right)_{i}} \right] \\ &+ \frac{1}{4} k_{1} \tan^{2} \theta \ln \left[\frac{\left(f \mu^{\frac{k_{2}}{k_{1}}} e^{\frac{2}{k_{1}} \varepsilon} \middle/ \rho^{\frac{1}{k_{1}}} \right)_{i+1}}{\left(f \mu^{\frac{k_{2}}{k_{1}}} e^{\frac{2}{k_{1}} \varepsilon} \middle/ \rho^{\frac{1}{k_{1}}} \right)_{i}} \right]. \end{split}$$

$$(A-17)$$

References

- Alemie, W., Sacchi, M.D., 2011. High-resolution three-term AVO inversion by means of a Trivariate Cauchy probability distribution. Geophysics 76 (3), R43–R55. https://doi.org/10.1190/1.3554627.
- Alkhalifah, T., Tsvankin, I., 1995. Velocity analysis for transversely isotropic media. Geophysics 60 (5), 1550–1566. https://doi.org/10.1190/1.1443888.
- Ayani, M., Grana, D., 2020. Statistical rock physics inversion of elastic and electrical properties for CO₂ sequestration studies. Geophys. J. Int. 223 (1), 707–724. https://doi.org/10.1093/gji/ggaa346.
- Baffoun, H., Hajlaoui, M., Farhat, A., 2017. Equation-solving estimator based on Metropolis-Hastings algorithm with delayed rejection. Commun. Stat. Simul. Comput. 46 (4), 3103–3111. https://doi.org/10.1080/03610918.2015.1073306.
- Banik, N.C., 1984. Velocity anisotropy of shales and depth estimation in the North Sea basin. Geophysics 49 (9), 1411–1419. https://doi.org/10.1190/1.1441770.
- Buland, A., Omre, H., 2003. Bayesian linearized AVO inversion. Geophysics 68 (1), 185–198. https://doi.org/10.1190/1.1543206.
- Carcione, J.M., 1997. Reflection and transmission of qP-qS plane waves at a plane boundary between viscoelastic transversely isotropic media. Geophys. J. Int. 129 (3), 669–680. https://doi.org/10.1111/j.1365-246X.1997.tb04502.x.
- Chen, F.B., Zong, Z.Y., 2022. PP-wave reflection coefficient in stress-induced anisotropic media and amplitude variation with incident angle and azimuth inversion. Geophysics 87 (6), C155–C172. https://doi.org/10.1190/geo2021-0706.1.
- Chen, F.B., Zong, Z.Y., Yin, X.Y., 2024a. Seismic scattering inversion for multiple parameters of overburden-stressed isotropic media. Geophysics 89 (6), 1–99. https://doi.org/10.1190/geo2023-0636.1.
- Chen, F.B., Zong, Z.Y., Lang, K., Li, J.Y., Yin, X.Y., Miao, Z.W., Xiao, W., 2024b. Geofluid discrimination in stress-induced anisotropic porous reservoirs using seismic AVAZ inversion. IEEE Trans. Geosci. Rem. Sens. https://doi.org/10.1109/ TGRS.2024.3477943.
- Chen, H.Z., Ji, Y.X., Innanen, K., 2018. Estimation of modified fluid factor and dry fracture weaknesses using azimuthal elastic impedance. Geophysics 83, WA73—WA88. https://doi.org/10.1190/geo2017-0075.1.
- Chen, H.Z., Zhang, G.Z., 2017. Estimation of dry fracture weakness, porosity, and fluid modulus using observable seismic reflection data in a gas-bearing reservoir. Surv. Geophys. 38, 651–678. https://doi.org/10.1007/s10712-017-9410-x.
- Crampin, S., 1981. A review of wave motion in anisotropic and cracked elastic-media. Wave Motion 3 (4), 343–391. https://doi.org/10.1016/0165-2125(81)
- Daley, P.F., Hron, F., 1977. Reflection and transmission coefficients for transversely isotropic media. Bull. Seismol. Soc. Am. 67 (3), 661–675. https://doi.org/ 10.1785/BSSA0670030661.
- Feng, Y.W., Zong, Z.Y., Zhang, G.Z., Lang, K., Chen, F.B., 2024. PP-wave reflection coefficient equation for HTI media incorporating squirt flow effect and frequency-dependent azimuthal AVO inversion for anisotropic fluid indicator. IEEE Trans. Geosci. Rem. Sens. https://doi.org/10.1109/TGRS.2024.3362816.
- Fu, X., 2024. Seismic amplitude inversion based on a new PP-wave reflection coefficient approximation equation for vertical transversely isotropic media. Geophysics 89 (3), R217–R230. https://doi.org/10.1190/geo2023-0132.1.
- Ge, Z.J., Pan, S.L., Liu, J.X., Zhou, J.Y., Pan, X.P., 2021. Estimation of brittleness and anisotropy parameters in transversely isotropic media with vertical axis of symmetry. IEEE Trans. Geosci. Rem. Sens. 60, 1–9. https://doi.org/10.1109/ TGRS.2021.3073162.
- Graebner, M., 1992. Plane-wave reflection and transmission coefficients for a transversely isotropic solid. Geophysics 57 (11), 1512–1519. https://doi.org/ 10.1190/1.1443219.
- Grana, D., Azevedo, L., De Figueiredo, L., Connolly, P., Mukerji, T., 2022. Probabilistic inversion of seismic data for reservoir petrophysical characterization. Review and examples. Geophysics 87 (5), M199–M216. https://doi.org/10.1190/ geo2021-0776.1.
- Jones, L.E., Wang, H.F., 1981. Ultrasonic velocities in Cretaceous shales from the Williston basin. Geophysics 46 (3), 288–297. https://doi.org/10.1190/1.1441199.
- Lang, K., Yin, X.Y., Zong, Z.Y., Qin, D., 2023. Anisotropic non-linear inversion based on a novel PP wave reflection coefficient for VTI media. IEEE Trans. Geosci. Rem. Sens. https://doi.org/10.1109/TGRS.2023.3295800.
- Li, K., Li, K., Yin, X.Y., Zong, Z.Y., 2022a. Hierarchical bayesian probabilistic seismic AVO inversion using Gibbs sampling with IA2RMS algorithm. Geosci. Rem. Sens. Lett. IEEE 19, 1–5. https://doi.org/10.1109/LGRS.2022.3181816.
- Li, K., Yin, X.Y., Zong, Z.Y., Grana, D., 2022b. Estimation of porosity, fluid bulk modulus, and stiff-pore volume fraction using a multitrace Bayesian amplitude-variation-with-offset petrophysics inversion in multiporosity reservoirs. Geophysics 87 (1), M25—M41. https://doi.org/10.1190/geo2021-0029.1.
- Li, L., Zhang, G.Z., Pan, X.P., Zhang, J.M., Zhu, Z.Y., Li, C., Lin, Z.L., 2022c. Bayesian amplitude variation with angle and azimuth inversion for direct estimates of a new brittleness indicator and fracture density. Geophysics 87 (5), M189—M197. https://doi.org/10.1190/geo2021-0767.1.
- Liang, F., Liu, C., Carroll, R., 2011. Advanced Markov Chain Monte Carlo Methods: Learning from Past Samples. John Wiley & Sons, United Kingdom.
- Lin, R.R., Thomsen, L., 2013. Extracting polar anisotropy parameters from seismic data and well logs. In: SEG Technical Program Expanded Abstracts 2013, pp. 310–314. https://doi.org/10.1190/segam2013-1150.1.
 Lu, J., Wang, Y., Chen, J.Y., An, Y., 2018. Joint anisotropic amplitude variation with
- Lu, J., Wang, Y., Chen, J.Y., An, Y., 2018. Joint anisotropic amplitude variation with offset inversion of PP and PS seismic data. Geophysics 83 (2), N31–N50. https:// doi.org/10.1190/geo2016-0516.1.

- Luo, C., Ba, J., Carcione, J.M., Huang, G.T., Guo, Q., 2020. Joint PP and PS pre-stack AVA inversion for VTI medium based on the exact Graebner equation. J. Pet. Sci. Eng. 194, 107416. https://doi.org/10.1016/j.petrol.2020.107416.
- Luo, K., Zong, Z.Y., Yin, X.Y., Cao, H., Lu, M., 2021. Bayesian Hamiltonian Monte Carlo method for the estimation of pyrolysis parameter S1. Geophysics 86 (6), M197–M209. https://doi.org/10.1190/geo2020-0795.1.
- Ma, Z.Q., Yin, X.Y., Zong, Z.Y., Tan, Y.Y., Ji, L.X., Yang, Z.F., Yan, X.F., 2023. Sequential Bayesian seismic inversion for fracture parameters and fluid indicator in tilted transversely isotropic media. Geophysics 88 (3), R355–R371. https://doi.org/10.1190/geo2022-0439.1.
- Marroquin, J.L., 1985. Probabilistic solution of inverse problems. In: Ph.D. Thesis. Massachusetts Institute of Technology, Cambridge, USA, pp. 16–18.
- Mosegaard, K, Tarantola, A, 1995. Monte Carlo sampling of solutions to inverse problems. J. Geophys. Res. Solid Earth. 100, 12431–12447. https://doi.org/10.1029/94IB03097.
- Pan, X.P., Zhang, G.Z., Yin, X.Y., 2019. Amplitude variation with offset and azimuth inversion for fluid indicator and fracture weaknesses in an oil-bearing fractured reservoir. Geophysics 84 (3), N41–N53. https://doi.org/10.1190/geo2018-0554.1.
- Plessix, R.E., Bork, J., 2000. Quantitative estimate of VTI parameters from AVA responses. Geophys. Prospect. 48 (1), 87–108. https://doi.org/10.1046/j.1365-2478.2000.00175.x.
- Rüger, A., 1998. Variation of P-wave reflectivity with offset and azimuth in anisotropic media. Geophysics 63 (3), 935–947. https://doi.org/10.1190/1.1444405.
- Russell, B.H., Gray, D., Hampson, D.P., 2011. Linearized AVO and poroelasticity. Geophysics 76 (3), C19—C29. https://doi.org/10.1190/1.3555082.
- Russell, B.H., Hedlin, K., Hilterman, F.J., Lines, L.R., 2003. Fluid-property discrimination with AVO: a Biot-Gassmann perspective. Geophysics 68 (1), 29–39. https://doi.org/10.1190/1.1543192.
- Sambridge, M., Mosegaard, K., 2002. Monte Carlo methods in geophysical inverse problems. Rev. Geophys. 40 (3), 31–329. https://doi.org/10.1029/2000RG000089
- Schoenberg, M., Protazio, J., 1990. "Zoeppritz" rationalized, and generalized to anisotropic media. J. Acoust. Soc. Am. 88 (S1), S46. https://doi.org/10.1121/1.2029011. S46.
- Shaw, R.K., Sen, M.K., 2004. Born integral, stationary phase and linearized reflection coefficients in weak anisotropic media. Geophys. J. Int. 158 (1), 225–238. https://doi.org/10.1111/j.1365-246X.2004.02283.x.
- Smith, G., Gidlow, P., 1987. Weighted stacking for rock property estimation and detection of gas. Geophys. Prospect. 35 (9), 993–1014. https://doi.org/10.1111/j.1365-2478.1987.tb00856.x.

- Thomsen, L., 1986. Weak elastic anisotropy. Geophysics 51 (10), 1954–1966. https://doi.org/10.1190/1.1442051.
- Ursin, B., Haugen, G.U., 1996. Weak-contrast approximation of the elastic scattering matrix in anisotropic media. Pure Appl. Geophys. 148, 685–714. https://doi.org/
- Vavrycuk, V., Psencík, I., 1998. PP-wave reflection coefficients in weakly anisotropic elastic media. Geophysics 63 (6), 2129–2141. https://doi.org/10.1190/1.1444506.
- Yang, Y.M., Yin, X.Y., Li, K., Zeng, Y.J., 2023. A linearized alternating direction method of multipliers algorithm for pre-stack seismic inversion in VTI media using the quadratic PP-reflectivity approximation. IEEE Trans. Geosci. Rem. Sens. https:// doi.org/10.1109/TGRS.2023.3267734.
- Yin, X.Y., Zhang, S.X., 2014. Bayesian inversion for effective pore-fluid bulk modulus based on fluid-matrix decoupled amplitude variation with offset approximation. Geophysics 79 (5), R221–R232. https://doi.org/10.1190/geo2013-0372.1.
- Yu, S.H., Zong, Z.Y., Yin, X.Y., Lang, K., Chen, F.B., 2023. Rock physics and seismic reflectivity parameterization and amplitude variation with offsets inversion in terms of total organic carbon indicator. Pet. Sci. 20 (4), 2092–2112. https:// doi.org/10.1016/j.petsci.2023.02.012.
- Zhang, F., Li, X., 2013. Generalized approximations of reflection coefficients in orthorhombic media. J. Geophys. Eng. 10 (5), 054004. https://doi.org/10.1088/1742-2132/10/5/054004.
- Zhang, F., Zhang, T., Li, X.Y., 2019. Seismic amplitude inversion for the transversely isotropic media with vertical axis of symmetry. Geophys. Prospect. 67 (9), 2368–2385. https://doi.org/10.1111/1365-2478.12842.
- Zhou, L., Chen, Z.C., Li, J.Y., Chen, X.H., Liu, X.Y., Liao, J.P., 2020. Nonlinear amplitude versus angle inversion for transversely isotropic media with vertical symmetry axis using new weak anisotropy approximation equations. Pet. Sci. 17, 628–644. https://doi.org/10.1007/s12182-020-00445-x.
- Zong, Z.Y., Yin, X.Y., 2017. Model parameterization and P-wave AVA direct inversion for Young's impedance. Pure Appl. Geophys. 174, 1965—1981. https://doi.org/ 10.1007/s00024-017-1529-7.
- Zong, Z.Y., Sun, Q.H., 2022. Density stability estimation method from pre-stack seismic data. J. Pet. Sci. Eng. 208, 109373. https://doi.org/10.1016/j.petrol.2021.109373. Zuo, Y.H., Zong, Z.Y., Li, K., Sun, Q.H., Yang, Y.M., 2023. Direct inversion for shale
- Zuo, Y.H., Zong, Z.Y., Li, K., Sun, Q.H., Yang, Y.M., 2023. Direct inversion for shale brittleness index using a delayed rejection adaptive Metropolis-Markov chain Monte Carlo method. Geophysics 88 (5), M225–M237. https://doi.org/10.1190/ pp.2022.05671
- Zuo, Y.H., Zong, Z.Y., Li, K., Luo, K., 2024. Bayesian AVOAz inversion of fluid and anisotropy parameters using Gibbs sampling with AISM algorithm. IEEE Trans. Geosci. Rem. Sens. 62, 1–15. https://doi.org/10.1109/TGRS.2024.3484435.